Assessing the variability in the relationship between the particulate backscattering coefficient and the chlorophyll *a* concentration from a global Biogeochemical-Argo database

Marie Barbieux[1], Julia Uitz[1], Annick Bricaud[1], Emanuele Organelli[1,2], Antoine Poteau[1], Catherine Schmechtig[3], Bernard Gentili[1], Christophe Penkerc'h[1], Edouard Leymarie[1], Fabrizio D'Ortenzio[1] & Hervé Claustre[1]

1-Sorbonne Universités, UPMC Univ Paris 06, CNRS, Observatoire Océanologique de Villefranche (OOV), Laboratoire d'Océanographie de Villefranche (LOV), 181 Chemin du Lazaret, 06 230 Villefranche-sur-Mer, France.

2- Plymouth Marine Laboratory, Prospect Place, The Hoe, PL1 3DH Plymouth, United Kingdom.

3- OSU Ecce Terra, UMS 3455, CNRS and Université Pierre et Marie Curie, Paris 6, 4 place Jussieu 75252 Paris cedex 05, France

Corresponding author: Marie Barbieux (barbieux@obs-vlfr.fr)

Key words: Particle backscattering, BGC-Argo profiling floats, optical properties, phytoplankton biomass, world's oceans

Key Points:

- The particulate backscattering coefficient *vs* chlorophyll *a* concentration relationship varies along the water column, according to seasons and oceanic regions.
- The b_{bp}-to-Chl*a* ratio is a valuable biogeochemical proxy for assessing the nature of the particulate assemblage and revealing photoacclimation processes.
- The BGC-Argo float network yields an unprecedented amount of quality data for studying biogeochemical processes at a global scale and along the vertical dimension.

Abstract:

Characterizing phytoplankton distribution and dynamics in the world's open oceans requires *in situ* observations over a broad range of space and time scales. In addition to temperature/salinity measurements, Biogeochemical-Argo (BGC-Argo) profiling floats are capable of autonomously observing at high frequency bio-optical properties such as the chlorophyll fluorescence, a proxy of the chlorophyll *a* concentration (Chl*a*), the particulate backscattering coefficient (b_{bp}), a proxy of the stock of particulate organic carbon, and the light available for photosynthesis. We analyzed an unprecedented BGC-Argo database of more than 8,500 multi-variable profiles collected in various oceanic conditions, from subpolar waters to subtropical gyres. Our objective is to refine previously established Chl*a* *vs* b_{bp} relationships and gain insights into the sources of vertical, seasonal and regional variability in this relationship. Despite some nuances in the relationship considering one or another water column layer or region, a general covariation occurs at a global scale. We distinguish two main contrasted situations: (1) concomitant changes in Chl*a* and b_{bp} that correspond to actual variations in phytoplankton biomass, e.g. in subpolar regimes; (2) a decoupling between the two variables attributed to photoacclimation or changes in the relative abundance of non-algal particles, e.g. in subtropical regimes. The variability in the b_{bp}:Chl*a* ratio in the surface layer appears to be essentially influenced by the type of particles and photoacclimation processes. The dense BGC-Argo database helps identifying the spatial and temporal scales at which this ratio is predominantly driven by one or the other of these two factors.

1 INTRODUCTION

Our ability to observe the dynamics of phytoplankton biomass and associated carbon fluxes on relevant space and time scales considerably limits our understanding and prediction skills of the biogeochemical role of phytoplankton in the carbon biological pump (*Volk and Hoffert*, 1985; *Honjo et al.*, 2014; *Legendre et al.*, 2015). For example, *in situ* measurements of primary production and phytoplankton carbon biomass are particularly challenging and remain scarce, although novel promising techniques have been recently proposed (*Riser and Johnson*, 2008; *Graff et al.*, 2012, 2015). To overcome space-time coverage sampling limitations, bio-optical oceanographers have implemented optical sensors on a variety of *in situ* or remote platforms, from research vessels and moorings to ocean color satellites, gliders and profiling floats, each with specific complementary space-time observation scales (*Dickey*, 2003; *Claustre et al.*, 2010). Such platforms enable to monitor bio-optical properties that serve as proxies for major biogeochemical variables. Those include the concentration of chlorophyll *a* (Chl*a*) and the particulate backscattering coefficient at 700 nm (hereafter referred simply as b_{bp}). The chlorophyll *a* concentration is the most commonly used proxy for the phytoplankton carbon biomass (*Cullen*, 1982; *Siegel et al.*, 2013), although it is well known that the ratio of Chl*a* to carbon shows large fluctuations driven by a variety of factors such as phytoplankton physiology (*Geider*, 1993; *Staehr et al.*, 2002; *Álvarez et al.*, 2016) or community composition (*Geider et al.*, 1997; *MacIntyre et al.*, 2002; *Halsey and Jones*, 2015). In the absence of mineral particles (*i.e.*, in most open-ocean waters), b_{bp} generally covaries with, and is therefore used as a proxy of, the stock of particulate organic carbon (POC) (*Stramski et al.*, 1999; *Loisel et al.*, 2002; *Bishop*, 2009). However changes in the nature (composition and size) of the particle assemblage may cause large variability in the b_{bp} signal and in the POC-to-b_{bp} relationship (*Flory et al.*, 2004; *Gardner et al.*, 2006; *Stramski et al.*, 2008; *Bishop*, 2009).

Examining bio-optical relationships, which for example link the inherent optical properties of particles such as absorption or scattering, to Chl*a*, has long been an area of active research in bio-optical oceanography (*Smith and Baker*, 1978a; *Mitchell and Holm-Hansen*, 1991; *Mitchell*, 1992; *Bricaud et al.*, 1995; *Morel et al.*, 2007b; *Szeto et al.*, 2011; *Huot and Antoine*, 2016; *Organelli et al.*, 2017a). Among different types of applications, bio-optical relationships enable deriving biogeochemical information over a broad range of space and time scales from *in situ* or remote optical measurements (*Loisel et al.*, 2002; *Siegel et al.*, 2005; *Huot et al.*, 2007b). Such relationships are also used in semi-analytical inverse models to interpret remote sensing ocean color data (*Gordon et al.*, 1988; *Loisel and Morel*, 1998; *Morel and Maritorena*, 2001). Various studies focused on the relationship between Chl*a* and b_{bp} using data from ocean color remote sensing (*Reynolds et al.*, 2001; *Stramska et al.*, 2003), field cruises (*Huot et al.*, 2008; *Dall'Olmo et al.*, 2009), fixed mooring (*Antoine et al.*, 2011), or Biogeochemical-Argo (BGC-Argo) profiling floats (*Xing et al.*, 2014). All of these studies confirmed the principle of the "bio-optical assumption" (*Smith and Baker*, 1978b; *Siegel et al.*, 2005), suggesting that in open-ocean waters the optical properties of a water mass co-vary to a first order with Chl*a*. Yet, depending on the considered data set, previous studies also indicate large second-order variability around the mean b_{bp} *vs*. Chl*a* power-law relationship (*Brown et al.*, 2008; *Huot et al.*, 2008; *Xing et al.*, 2014). Restricted to a given period of time, region or trophic regime and mainly to the surface layer of the water column, these studies did not lead to a thorough characterization of the variability in the relationship between Chl*a* and b_{bp} over the full range of environments encountered in the open ocean. In addition, these studies involved different methodologies for b_{bp} measurements or retrievals, so that it is difficult to untangle regional and/or seasonal variability from possible methodological biases (*Sullivan et al.*, 2013).

The recently launched network of BGC-Argo profiling floats is progressively transforming our capability to observe optical properties and biogeochemical processes in the oceans (*Claustre et al.*, 2010; *IOCCG*, 2011; *Biogeochemical-Argo Planning Group*, 2016; *Johnson and Claustre*, 2016). The current BGC-Argo bio-optical database has drastically increased over recent years and now encompasses observations collected in a broad range of hydrological, trophic and bio-optical conditions encountered in the world's open oceans (*Organelli et al.*, 2017a, 2017b). Based on homogeneous measurements and processing methodologies, this database offers a unique opportunity to comprehensively reassess bio-optical relationships. Based on the analysis of more than 8500 multi-variable profiles collected within the water column (0–1000 m) by BGC-Argo floats, this study aims to (i) investigate the natural variability around the mean statistical b_{bp}-to-Chl*a* relationship at the vertical, regional and seasonal scales and (ii) identify the underlying sources of variability.

2 DATA AND METHODS

2.1 BGC-Argo profiling floats

2.1.1 BGC-Argo database

An array of 105 BGC-Argo profiling floats was deployed in several areas of the world's oceans in the frame of several research programs (*Organelli et al.*, 2016a, 2017a). BGC-Argo profiling float real-time data are accessible online (at ftp://ftp.ifremer.fr/ifremer/argo/dac/coriolis/), distributed as netCDF data files (*Wong et al.*, 2013) and updated daily with new profiles. The quality-controlled database of bio-optical vertical profiles that supports this work is publicly available from SEANOE (SEA scieNtific Open data Edition) publisher (*Barbieux et al.*, 2017). In this database, profiles of b_{bp} were eliminated when bathymetry was shallower than 400 m and a signature of b_{bp} at depth was

noticeable. This allowed us to remove the data collected in waters where a coastal influence was suspected, Black Sea excepted. Hence 8908 BGC-Argo multi-parameter profiles or "stations" (corresponding to 91 different BGC-floats) collected between November 8, 2012 and January 5, 2016, were used in this study. These stations were grouped into 24 geographic areas (Table 1), following the bioregions presented in *Organelli et al.* (2017a), except for the Eastern Subtropical Atlantic Gyre that is missing in our database because of suspicious backscattering data from the two profiling floats deployed in this bioregion. In this paper, we show the graphs and data for each of these 24 bioregions so that each reader can evaluate the variability in the b_{bp}:Chla ratio for any specific region of interest.

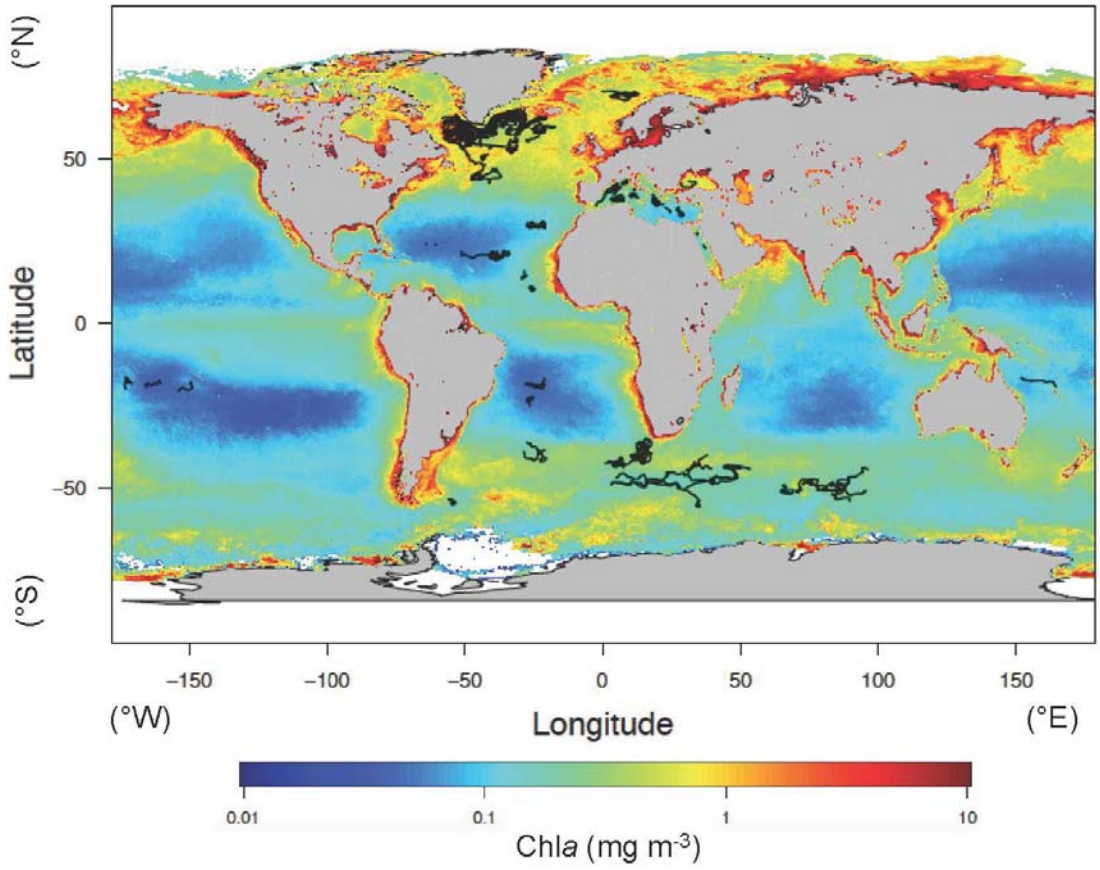

Figure 1: *Geographical location of the multi-variable vertical profiles collected by the BGC-Argo profiling floats represented in the database used in this study. The geographic locations are superimposed on an annual climatology of the surface chlorophyll a concentration derived from MODIS-Aqua climatological observations for the year 2015 (https://oceancolor.gsfc.nasa.gov/cgi/l3).*

Our database includes measurements from a wide range of oceanic conditions, from subpolar to tropical waters and from eutrophic to oligotrophic conditions (Fig. 1). For the purpose of simplifying the presentation of the results, we grouped the different bioregions into five main regimes: (1) the North Atlantic Subpolar Gyre (NSPG) divided in Icelandic basin, Labrador and Irminger Seas; (2) the Southern Ocean (SO) essentially comprising the Indian and the Atlantic sectors; (3) the Mediterranean Sea (MED) that comprises the Northwestern basin (NW_MED), the Southwestern basin (SW_MED), the Tyrrhenian Sea (TYR_MED), the Ionian Sea (ION_MED) and the Levantine Sea (LEV_MED); (4) the subtropical regimes (STG) that include subtropical oligotrophic waters from the North and South Atlantic and Pacific Oceans and Red Sea (RED_SEA); and (5) the Black Sea (Table 1).

Table 1. Bioregions with the corresponding abbreviation, regime and number of available floats and profiles represented in the BGC-Argo database used in the present study.

Bioregion	Abbreviation	Regime	Number of profiles	Number of floats
Norwegian Sea	NOR_ARC	North Subpolar Gyre (NSPG)	139	1
Icelandic Basin	ICB_NASPG		828	8
Irminger Sea	IRM_NASPG		623	11
Labrador Sea	LAS_NASPG		1160	16
South Labrador Sea	SLAS_NASPG		62	2
North Atlantic Transition Zone to northern border of the Subtropical Gyre	STZ_NASPG		146	1
Atlantic to Indian Southern Ocean	ATOI_SO	Southern Ocean (SO)	910	10
Indian Sector of the Southern Ocean	IND_SO		653	6
Atlantic Sector of the Southern Ocean	ATL_SO		49	1
Ligurian Sea & Gulf of Lions	NW_MED	Mediterranean Sea (MED)	698	8
Provencal & Algero-provencal basin	SW_MED		417	4
Tyrrhenian Sea	TYR_MED		325	5
Ionian Sea	ION_MED		499	6
Levantine Sea	LEV_MED		511	7
Red Sea	RED_SEA	Subtropical Gyre (STG)	75	2
North Atlantic Western Subtropical Gyre	WNASTG		12	2
South Atlantic South Subtropical Gyre	SSASTG		108	1
North Atlantic Subtropical Gyre	NASTG		363	4
South Pacific Subtropical Gyre	SPSTG		281	3
New Caledonia Sector of the Pacific	NC_PAC		139	2
South Atlantic Subtropical Gyre	SASTG		368	2
South Atlantic Subtropical Transition Zone	SASTZ		214	2
North Atlantic Transition Zone to Subtropical Equatorial Atlantic	EQNASTZ		187	2
Black Sea	BLACK_SEA	BLACK_SEA	141	2

2.1.2 Biogeochemical-Argo sensor characteristics and sampling strategy

The 'PROVOR CTS-4' (NKE Marine Electronics Inc., France) is a profiling autonomous platform specifically designed in the context of the Remotely-Sensed Biogeochemical Cycles in the Ocean (remOcean) and Novel Argo Ocean Observing System (NAOS) projects. The PROVOR CTS-4 profiling floats used in this study were equipped with a SBE 41 CTD (Seabird Inc., USA), an OCR-504 (SAtlantic Inc., USA) multispectral radiometer measuring the Photosynthetically Available Radiation over the 400–700 nm range (PAR), and an ECO3 (Combined Three Channel Sensors; WET Labs, Inc., USA) measuring the fluorescence of chlorophyll *a* and Colored Dissolved Organic Matter (CDOM) at excitation/emission wavelengths of 470/695 nm and 370/460 nm respectively, and the angular scattering coefficient of particles ($\beta(\theta, \lambda)$) measured at 700 nm and an angle of 124°. Measurements were collected during upward casts programmed every 1, 2, 3, 5, or 10 days depending on the mission and scientific objectives. All casts started from the parking depth at 1000 m at a time that was sufficient for surfacing around local noon. Vertical resolution of acquisition was 10 m between 1000 m and 250 m, 1 m between 250 m and 10 m, and 0.2 m between 10 m and the surface (*Organelli et al.*, 2016a). Raw data (electronic counts) were transmitted to land, each time the floats surfaced, through Iridium two-way communication, and were converted into desired quantities. Each variable was quality-controlled according to procedures described hereafter and specifically developed for BGC-Argo data (*Schmechtig et al.*, 2014, 2016; *Organelli et al.*, 2016b). Additionally, all the casts were checked for data degradation due to bio-fouling or instrumental drift.

2.2 Bio-optical data processing

2.2.1 Chlorophyll *a* concentration

After dark counts have been subtracted from the raw signal, chlorophyll *a* fluorescence was first converted into chlorophyll *a* concentration according to calibration coefficients provided by the manufacturer (*WET Labs*, 2016). Following the procedures described in *Schmechtig et al.* (2014), the real-time dedicated quality control procedure identified the occurrence of negative spikes, adjusted chlorophyll *a* concentration profiles for cases of non-zero values at depth and verified the range of measured values according to technical specifications provided by the manufacturer (*WET Labs*, 2016). In order to correct for the effect of the so-called non-photochemical quenching (NPQ) (decrease in the fluorescence-to-Chl*a* ratio under high light conditions) (*Kiefer et al.*, 1973), we systematically applied the procedure developed by *Xing et al.* (2012). Besides, in some bioregions such as subtropical gyres or the Black Sea, the chlorophyll *a* concentration appeared to increase at depth where it should be null. *Proctor and Roesler* (2010) assigned this behavior to the influence of fluorescence originating from non-algal matter. Profiles were thus corrected according to *Xing et al.* (2016). Finally, following the recommendation by *Roesler et al.* (2017) for Chl*a* measurements from WET Labs ECO fluorometers, the calibrated quality-controlled Chl*a* values were divided by a correction factor of 2. The correction factor was deducted from a global comparison of paired HPLC (High Performance Liquid Chromatography) and *in situ* fluorescence Chl*a* data, and confirmed by optical proxies of Chl*a* such as light absorption line height (*Roesler and Barnard*, 2013) or *in situ* radiometry (*Xing et al.*, 2011). The regional variability of this average correction factor along with its possible uncertainties is fully discussed in *Roesler et al.* (2017). We performed a sensitivity analysis of the b_{bp}-to-Chl*a* relationship to the factor used for correcting the fluorescence-based Chl*a* values. We tested the influence of using two sets of regional factors proposed by *Roesler et al.* (2017) derived either from HPLC analyses

or radiometric measurements, compared to the global factor of 2. Except for the Southern Ocean that appears more sensitive than other regions to the choice of the correction factor, our analysis reveals that the regional factors induce minor changes to the b_{bp}-to-Chl*a* relationship. Overall those minor changes have little impact on the interpretation of our results. Thereafter our analysis considers Chl*a* values originating from the global correction factor. Details of the sensitivity analysis may be found in supporting information SA presented as electronic supplementary material.

2.2.2 Particulate backscattering coefficient

We followed the procedure established by *Schmechtig et al.* (2016). Backscattering sensors implemented on floats provide the angular scattering coefficient β at 124° and at 700 nm. The particulate backscattering coefficient was calculated following *Boss and Pegau* (2001):

$$b_{bp}(700)\ (m^{-1}) = \chi(124) \times 2\pi \times \{\beta(124,700) - \beta_{sw}(124,700)\} \quad (1)$$

with $\beta(124,700)\ (m^{-1}\ sr^{-1}) = \text{slope} \times (\text{counts} - b_b\text{dark})$

where the (instrument-specific) slope and $b_b$dark are provided by the manufacturer, and $\chi(124)$ is equal to 1.076 (*Sullivan et al.* 2013). The contribution of pure seawater (β_{sw}), was removed in order to take into account the effect of the temperature and salinity and was computed according to *Zhang et al.* (2009). Finally, vertical profiles were quality-controlled by verifying the range of measured values according to the technical specifications provided by the manufacturer (*WET Labs*, 2016) and removing negative spikes following *Briggs et al.* (2011). Remaining spikes were removed by applying a median filter (5-point window).

2.2.3 Estimation of uncertainty in the b_{bp}-to-Chl*a* ratio

The backscattering and chlorophyll fluorescence sensors implemented on floats are all ECO3 sensors (WET Labs, Inc.). This avoids heterogeneous sources of uncertainties associated with

various sensors (see, e.g., (*Roesler et al.*, 2017)). In addition, the data are calibrated and qualified following the recommended standard BGC-Argo procedure presented in Schmechtig et al. (2016). A thorough estimation of the uncertainties affecting the different parameters would necessitate an entirely dedicated study, which is beyond the scope of the present one. However, an estimation of the average error that may influence our results has been made.

Accounting for measurement error only, we assume an error $\sigma\, b_{bp}(700)(m^{-1}) = 2.2 \times 10^{-6}$ for the b_{bp} sensor and $\sigma\, \mathrm{Chl}a\ (\mathrm{mg\ m^{-3}}) = 0.007$ for the chlorophyll fluorescence sensor, as provided by the manufacturer. Following an error propagation law (*Birge*, 1939; *Ku*, 1966), the combined effect of these errors on the b_{bp}-to-Chla ratio can be computed and a relative error (in %) can be obtained as:

$$\sigma\left[b_{bp}/\mathrm{Chla}\right] = \sqrt{\frac{\sigma\, b_{bp}{}^{2}}{\mathrm{Chla}^{2}} + \frac{b_{bp}{}^{2} \times \sigma\, \mathrm{Chla}^{2}}{\mathrm{Chla}^{4}} - \frac{2 \times b_{bp} \times \mathrm{cor}\left(b_{bp}, \mathrm{Chla}\right) \times \sigma\, b_{bp} \times \sigma\, \mathrm{Chla}}{\mathrm{Chla}^{3}}}{b_{bp}} \times \mathrm{Chla} \qquad (2)$$

Considering the surface data, a median error of 0.11% is obtained and 80% of the data show relative errors lower than 10% (Fig. 2a). Relative errors larger than 10% appear for the lowest values of b_{bp} ($<10^{-3}$ m^{-1}) and Chl*a* ($<10^{-2}$ mg m-3) (Fig. 2b), which corresponds to the clearest waters of the oligotrophic gyres. In addition, a sensitivity analysis described in supporting information SA indicates that correcting the fluorescence-based Chl*a* values of the database with regional factors compared to a global factor does not significantly affect the distribution of the computed errors in the b_{bp}-to-Chl*a* ratio (see electronic auxiliary material).

2.3 Derived variables

2.3.1 Physical and biogeochemical layers of the water column

We consider four different layers of the water column: (i) the productive layer (*Morel and Berthon*, 1989) comprised between the surface and 1.5 Z_{eu}, with Z_{eu} corresponding to the

239 euphotic depth which is the depth at which PAR is reduced to 1% of its surface value; (ii) the
240 mixed layer where all properties are expected to be homogenous and that encompasses a large
241 fraction of the phytoplankton biomass (*Brainerd and Gregg*, 1995; *Taylor and Ferrari*,
242 2010); (iii) the surface layer, observable by satellite remote sensing, extending from surface to
243 the first optical depth (Z_{pd}) (Gordon and McCluney, 1975); and (iv) the deep chlorophyll
244 maximum (DCM) layer (i.e. thickness of the DCM) where different processes may lead to a
245 Chl*a* enhancement. Unlike the productive layer, the surface, the mixed and the deep
246 chlorophyll maximum layers are considered as homogeneous layers where the phytoplankton
247 population is expected to be acclimated to the same light and nutrient regimes. The 0-1.5 Z_{eu}
248 layer is chosen to estimate the average b_{bp}-to-Chla ratio in the entire enlightened layer of the
249 water column, even if it is acknowledged that large variations in this ratio may occur
250 throughout this layer. This average b_{bp}-to-Chla ratio is thereafter used as a reference to which
251 we compare the ratios calculated for the other layers of the water column.

252 The Mixed layer depth (MLD) was determined using a 0.03 kg m^{-3} density criterion (*de*
253 *Boyer Montégut*, 2004). The euphotic depth Z_{eu} and the penetration depth, $Z_{pd} = Z_{eu}/4.6$, were
254 computed from the BGC-Argo PAR vertical profiles following the procedure described in
255 *Organelli et al.* (2016b). Values of Z_{eu} and Z_{pd} are available from *Organelli et al.* (2016a). To
256 study more specifically the dynamics of the bio-optical properties in the DCM layer and
257 because the width of a DCM may fluctuate in space and time, we adjusted a Gaussian profile
258 to each vertical profile of Chl*a* of the database that presented a deep Chl*a* maximum and
259 computed the width of this DCM. This parameterizing approach proposed by *Lewis et al.*
260 (1983) has been widely used to fit vertical profiles of Chl*a* (e.g. *Morel and Berthon*, 1989;
261 *Uitz et al.*, 2006) such as:

262 $$c(z) = c_{max}\, e^{-\left(\left(\frac{z-z_{max}}{\Delta z}\right)^2\right)} \qquad (2)$$

where c(z) is the Chl*a* concentration at depth z, c_{max} is the Chl*a* concentration at the depth of the DCM (z_{max}) and Δz, the unknown, is the width of the DCM.

In order to retrieve Δ*z*, the unknown parameter, we performed an optimization of Eq. (2) with a maximum width set at 50 m so only the profiles with a relatively pronounced DCM are kept. Then we computed the mean Chl*a* and b_{bp} for the layer that represents the thickness of the DCM. Finally, all quality-controlled profiles of Chl*a* and particulate backscattering coefficient were averaged within the different considered layers.

2.3.2 Environmental and biological parameters

In order to analyze the variability in the b_{bp}-to-Chl*a* relationship, we consider the role of the light conditions in the various layers of the water column, i.e. the productive, mixed, surface and DCM layers. The vertical profiles of b_{bp}:Chl*a* and PAR were averaged within each of the four considered layers. For each layer, both variables the median value was computed monthly and regionally (i.e. for each regime). For each layer and each regime, we determined the maximum observed PAR that was used to normalize the monthly median PAR values of the corresponding layer and regime (PAR_{norm}). Ultimately, for each layer and each regime, the monthly median PAR_{norm} values were classified into four different intervals (0-0.25; 0.25-0.50; 0.50-0.75; 0.75-1), and the monthly-averaged b_{bp}: Chl*a* values were assigned to one of these four PAR_{norm} intervals.

Using the method of *Uitz et al.* (2006)), an index of the phytoplankton community composition, based on the relative contributions of size classes to total chlorophyll *a*, was also computed from the surface Chl*a* values. We applied this procedure to the surface Chl*a* values from our BGC-Argo database, that we further monthly averaged to finally obtain the relative contributions of micro-, nano- and picophytoplankton to the total chlorophyll *a* biomass for each bioregion within the 0-Z_{pd} layer.

3 RESULTS

3.1 Overview of the BGC-Argo database

A latitudinal decreasing gradient of surface Chl*a* is observed from the North Subpolar Gyre (NSPG) and Southern Ocean (SO) regimes to the subtropical (STG) regime with a median Chl*a* from ~1 mg m^{-3} to ~0.05 mg m^{-3}, respectively (Fig. 2a). It is noteworthy that, in our dataset where the South East Pacific Ocean is not represented, the South Atlantic Subtropical Gyre (SASTG) is the most oligotrophic bioregion, experiencing the lowest median Chl*a* (0.014 mg m^{-3}) and the highest median Z_{eu} (135 m). A west-to-east trophic gradient is observed in the Mediterranean Sea, with median surface Chl*a* values of 0.186 mg m^{-3} and 0.025 mg m^{-3} in the Northwestern Basin and the Levantine Sea, respectively (Fig. 2a).

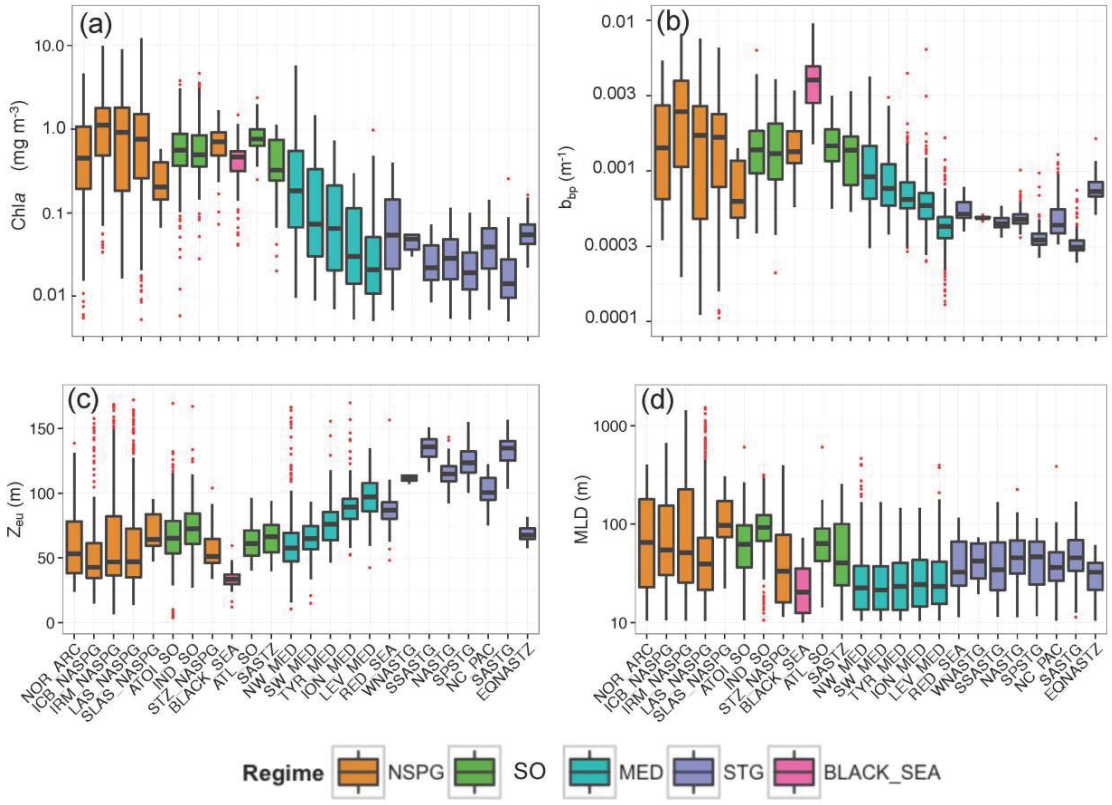

Figure 2: *Boxplot of the distribution, for each of the 24 bioregions represented in the BGC-Argo database used in this study, of the (a) chlorophyll a concentration (Chla) in the surface*

(0-Z_{pd}) layer; (b) particulate backscattering coefficient at 700 nm (b_{bp}) in the surface (0-Z_{pd}) layer; (c) depth of the euphotic layer (Z_{eu}); and (d) mixed layer depth (MLD). Note that the bioregions are ordered following the absolute value of the latitude and, within the Mediterranean Sea, following the longitude (i.e. from west to east). Red points beyond the end of the whiskers represent outliers beyond the 1.5 x IQR (IQR = Interquartile range) threshold.

A similar pattern is observed in the surface particulate backscattering coefficient values (Fig. 2b). Median surface b_{bp} values range between ~0.002 m^{-1} in NSPG and ~0.0003 m^{-1} in STG regime. In the Mediterranean Sea, the b_{bp} values vary over one order of magnitude, with maximum values found in the Northwestern Basin and minimum values in the Levantine Sea. The North Atlantic Transition Zone to Subtropical Equatorial Atlantic (EQNASTZ) bioregion exhibits particularly high values of b_{bp} compared to other STG regions (Fig. 2a). The Z_{eu} values also show a latitudinal gradient (Fig. 2c), with median values of ~50 m in NSPG and ~125 m in STG regimes. The median MLD shows a significant variability among the 24 bioregions (Fig. 2d). The distribution of the MLD in the Mediterranean Sea is centered on a low median value of 23 m, but very large values (>250 m) are episodically observed in the Northwestern Mediterranean (NW_MED). The deepest mixed layers (median value of 98 m) are observed in the South Labrador Sea (SLAS_NASPG), and episodes of extremely deep mixed layers (~1000 m) are also recorded in the Labrador Sea (LAS_NASPG). The shallowest mixed layers are observed in the Black Sea (~20 m). It is also worth to notice that MLD values in STG are particularly stable and feature very few outliers.

3.2 Variability in the b_{bp}-to-Chl*a* relationship at the global scale within distinct layers of the water column

3.2.1 The productive layer

In this layer, the b_{bp}-to-Chl*a* relationship follows a power law ($R^2 = 0.74$) (Fig. 3a). Yet when data from different regimes and bioregions are considered separately, regional and seasonal patterns emerge. Bioregions of the subpolar NSPG and SO regimes (Figs. 4a–i) show a significant correlation between Chl*a* and b_{bp} with high R^2 (> 0.60) and slope (i.e. exponent of the power law) always above 0.50 (except for the Norwegian Sea, Fig. 4a). Minimal values of both Chl*a* and b_{bp} are encountered in winter whereas maximal values are reached in summer. Deviations from the global log-log linear model occur in some bioregions of the NSPG regime, e.g. in the Icelandic Basin (ICB_NASPG) in summer (Fig. 4b) and are characterized by an abnormally high b_{bp} signal considering the observed Chl*a* levels. Such a deviation is found all year long in the Black Sea, where a correlation between Chl*a* and b_{bp} is no longer observable ($R^2 = 0.09$) (Fig. 4x).

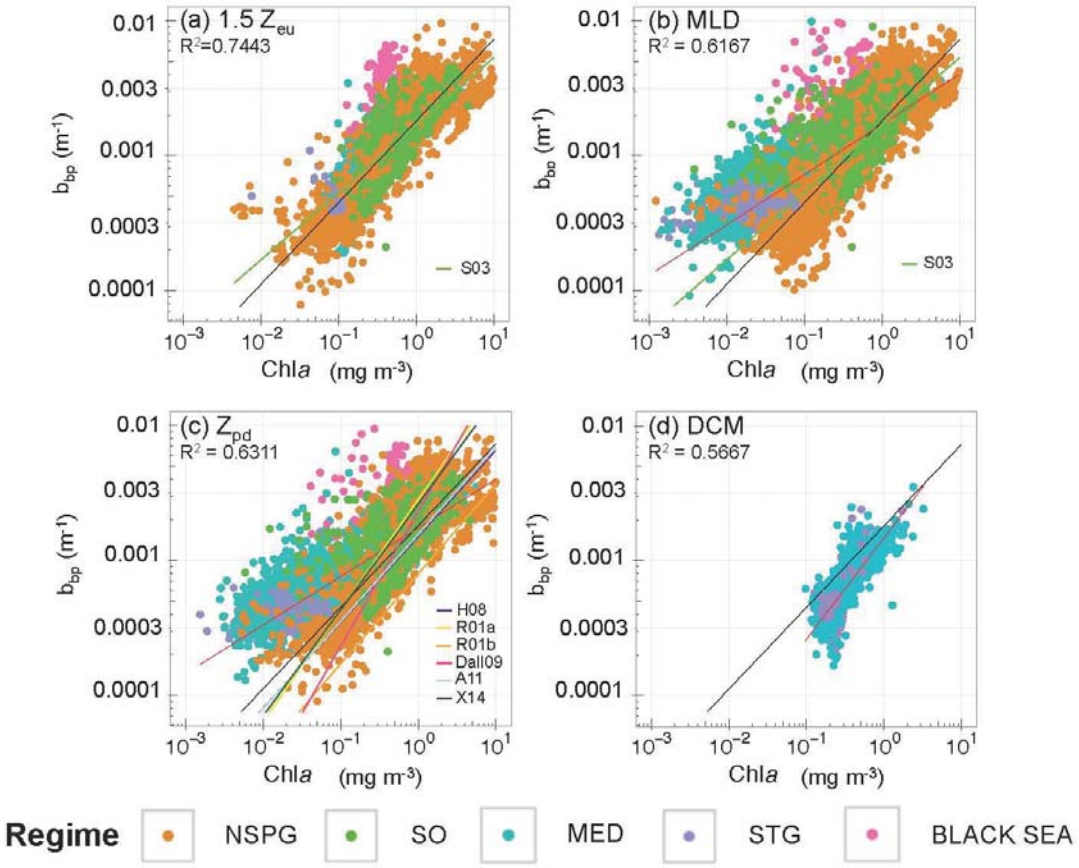

Figure 3: *Log-log scatterplot of the particulate backscattering coefficient at 700 nm (b_{bp}) as a function of the chlorophyll a concentration (Chla) within (a) the productive layer comprised between the surface and 1.5 Z_{eu}; (b) the mixed layer; (c) the surface (0-Z_{pd}) layer; and (d) at the level of the deep chlorophyll maximum (DCM). The color code indicates the regime where the Biogeochemical-Argo data were collected. For each plot, the black line represents the relationship calculated over the productive layer (0-1.5 Z_{eu}) while the red line the regression model calculated over the considered layer. The other lines represent regression relationships from the literature summarized in Table 2.*

Table 2. Empirical relationship between the particulate backscattering coefficient (b_{bp}) and the concentration of chlorophyll *a* (Chl*a*) previously published in the literature with the corresponding reference and abbreviation, region and layer of the water column considered for analysis.

Empirical relationship	Region	Layer in the water column	Abbreviation	Reference
$b_{bp}(\lambda) = 0.0023 - 0.000005 (\lambda - 550) Chla^{0.565+0.000486 (\lambda-550)}$	Eastern South Pacific	$2/K_d(490)$	H08	Huot et al. (2008)
$b_{bp}(555) = 0.004 Chla^{0.822}$	Antarctic Polar Front	15m	R01a	Reynolds et al. (2001)
$b_{bp}(555) = 0.001 Chla^{0.667}$	Ross Sea	15m	R01b	Reynolds et al. (2001)
$b_{bp}(555) = 0.0019 Chla^{0.61}$	Polar North Atlantic	MLD	S03	Stramska et al. (2003)
$b_{bp}(526) = 0.00386 Chla$	Eastern Equatorial Pacific	Surface	Dall09	Dall'Olmo et al. (2009) modified in Xing et al. (2014)
$b_{bp}(532) = 0.003 Chla^{0.786}$	North Atlantic Subpolar Gyre	Z_{pd}	X14	Xing et al. (2014)
$b_{bp}(555) = 0.00197 Chla^{0.647}$	North-western Mediterranean Sea and Santa Barbara Channel	Surface	A11	Antoine et al. (2011)

346 In the Mediterranean Sea, the slope and R^2 decrease from the Northwestern Basin
347 (NW_MED, Fig. 4j) to the Levantine Sea (LEV_MED, Fig. 4n), where Chl*a* appears to be
348 decoupled from b_{bp}. In the Mediterranean Sea, a seasonal pattern is noticeable principally in
349 the NW_MED, where the highest values of Chl*a* and b_{bp} are found in spring. Except for the
350 South Atlantic Subtropical Transition Zone (SASTZ) that displays a steep slope and a high R^2
351 value (0.68 and 0.80, respectively), regions from the subtropical regime do not show any
352 significant correlation between Chl*a* and b_{bp}, featuring the lowest slope and R^2 values of the
353 b_{bp}-to-Chl*a* relationship (Figs. 4o-w). This clearly suggests a decoupling between those two
354 properties. In these oligotrophic environments, different production regimes are delineated
355 along the vertical axis in the upper and lower part of the euphotic zone. One may expect that
356 the b_{bp}-to-Chl*a* relationship will vary depending on the considered layer. In this perspective,
357 we further investigate the behavior of the bio-optical properties in different layers of the water
358 column, namely the mixed layer, the surface layer and the DCM layer.

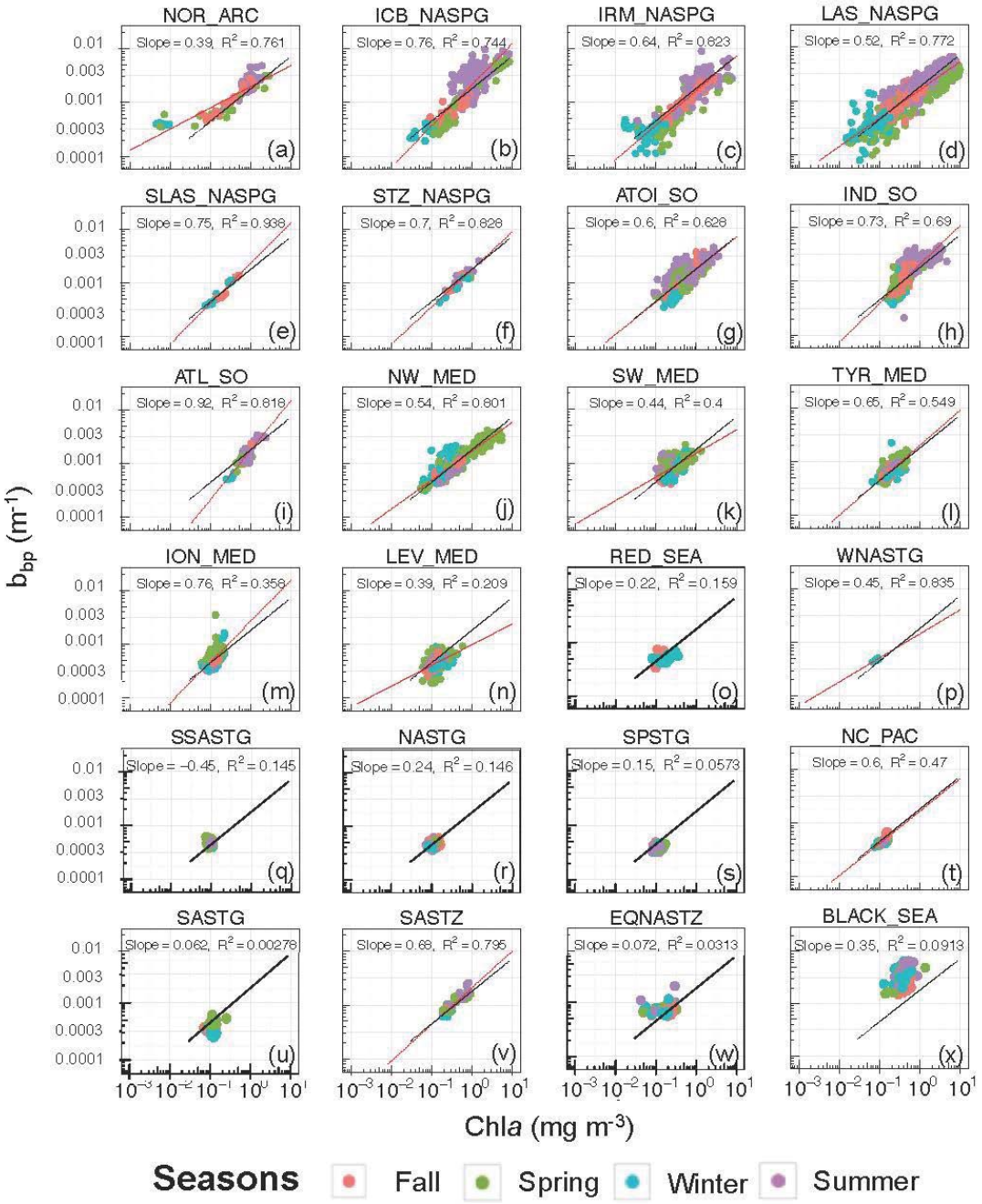

Figure 4: *Log-log scatterplot of the particulate backscattering coefficient at 700 nm (b_{bp}) as a function of the chlorophyll a concentration (Chla) within the layer comprised between the surface and 1.5 Z_{eu} for each bioregion. The color code indicates the seasons. The black line represent the average relationship calculated in this layer all bioregions combined and the red line corresponds to the regression model calculated for each bioregion considered here (when R^2>0.2).*

3.2.2 The mixed and surface layers

The distribution of Chl*a* and b_{bp} data for the surface and mixed layers show similar patterns (Figs. 3b–c). The distribution in the surface layer shows two distinct trends. With the exception of the Atlantic to Indian Southern Ocean (ATOI_SO) bioregion that shows an important dispersion of b_{bp} values during summer, the data collected in the NSPG and SO regimes and NW_MED bioregions exhibit a clear log-log linear covariation between Chl*a* and b_{bp} associated with slopes above 0.3 and high R^2 (Figs. 5a-j), similarly to what is observed for the productive layer (Figs. 3a and 4). In the subpolar NSPG and SO regimes, values of b_{bp} and Chl*a* in the 0-Z_{pd} layer reach their maximal values in summer (Fig. 5a-i) whereas in the NW_MED the highest values are recorded in spring (Fig. 5j). Data from the subtropical regime (STG) form a separate cluster where Chl*a* and b_{bp} are decoupled, with generally very low R^2 values. Chl*a* values encountered are almost always under 0.1 mg m^{-3} and the slope of the relationship remains under 0.2. Whereas b_{bp} values remain constant all over the seasons, a seasonal increase of Chl*a* is observable with noticeable higher winter values (Figs. 5o-w).

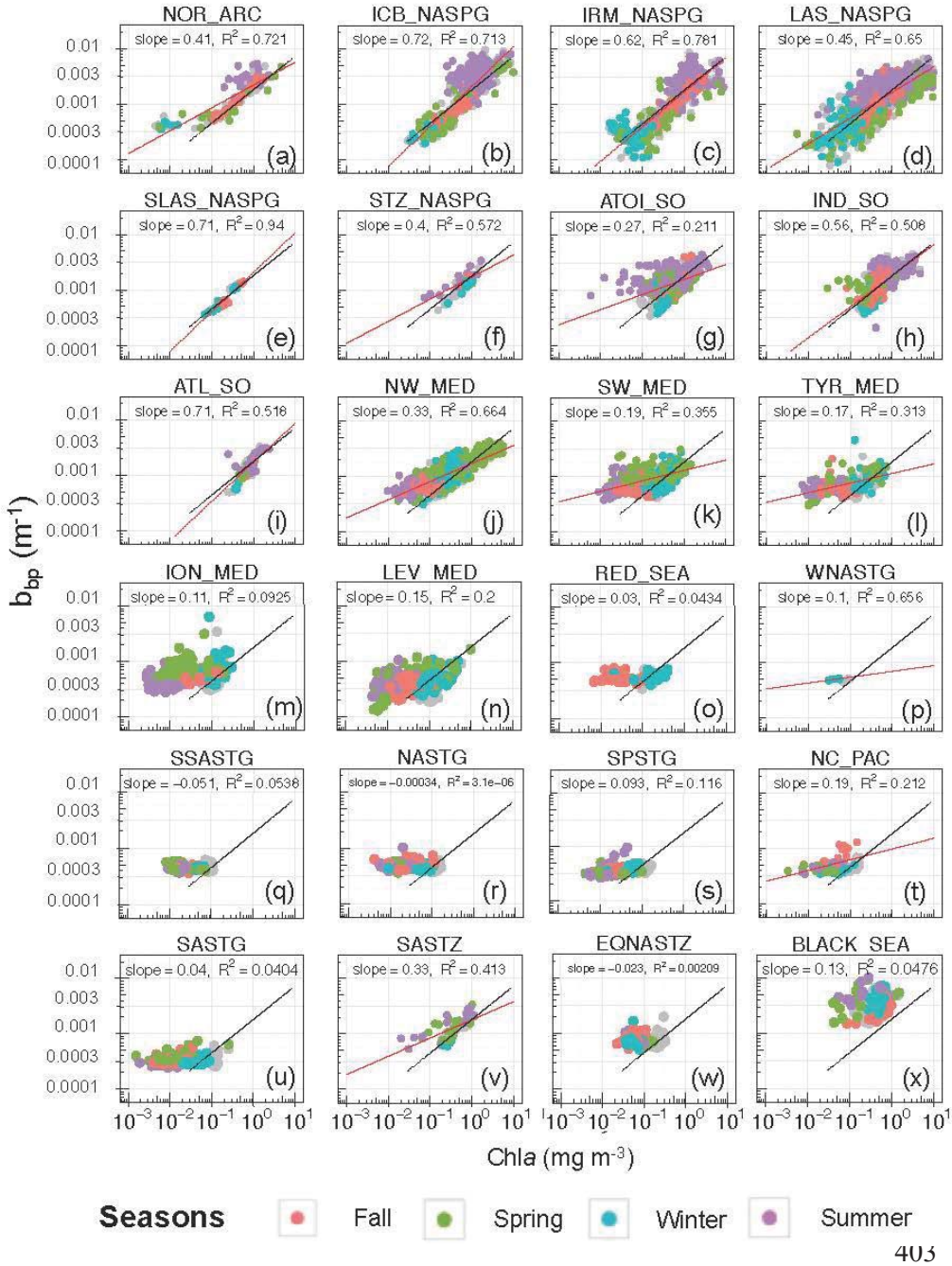

403

404 **Figure 5**: *Log-log scatterplot of the particulate backscattering coefficient at 700 nm (b_{bp}) as a*
405 *function of the chlorophyll a concentration (Chla) within the surface layer (0-Z_{pd}) for each*
406 *bioregion. The color code indicates the seasons. For each plot, the black line represents the*
407 *average relationship calculated for the surface layer (0-Z_{pd}) for the entire database while the*
408 *red line is the regression model calculated for each bioregion (shown only if R^2>0.2). The*
409 *data points for the productive layer are shown in grey color.*

410

411 The MED Sea is characterized by a gradual decrease in the Chl*a* and b_{bp} covariation
412 across a longitudinal trophic gradient (Figs. 5j-n) from the NW_MED (slope = 0.33, R^2 =
413 0.66) to the LEV_MED (slope = 0.15, R^2 = 0.21). The Eastern Mediterranean basin does not
414 feature any spring maximum in Chl*a* and b_{bp} (Figs. 5m,n). However, there is a noticeable
415 winter increase in Chl*a* as in the STG regime. Regarding the Black Sea bioregion, high values
416 of both variables are observed and no seasonal pattern is noticed (Fig. 5x), consistent with
417 what is observed in the productive layer.

418 **3.2.3 The Deep Chlorophyll Maximum layer**

419 The analysis of the b_{bp}-to-Chl*a* relationship at the level of the DCM obviously considers only
420 the seasonal or permanent stratified regimes (and bioregions) where a DCM occurs, i.e. the
421 Mediterranean and subtropical regimes. The b_{bp}-to-Chl*a* relationship in the DCM layer
422 gradually deviates from the relationship established in the productive layer all regions
423 combined (Fig. 3d). Chl*a* is systematically higher by a factor ~2 regardless of the bioregion
424 and never reaches values below 0.1 mg m^{-3} (Figs. 3d and Fig. SB1 of supporting information
425 SB).

426 The subset of data from this layer also shows two distinct trends in the b_{bp}-to-Chl*a*
427 relationship, for Chl*a* values below or above 0.3 mg m^{-3} (Fig. 3d). For Chl*a* > 0.3 mg m^{-3}, a
428 positive correlation between b_{bp} and Chl*a* can be noticed, although with a large dispersion of
429 the data around the regression line, whereas for Chl*a* < 0.3 mg m^{-3}, Chl*a* and b_{bp} exhibit a
430 strong decoupling. The MED Sea (Figs. SB1a-e) is characterized by a stronger covariation
431 between Chl*a* and b_{bp} than the STG regime (Figs. SB1g-n) (R^2 = 0.53 for NW_MED versus
432 R^2 = 0.10 for SPSTG). In the Mediterranean Sea, DCMs are seasonal phenomena occurring
433 essentially in summer or fall (e.g., *Siokou-Frangou et al.*, 2010). A covariation between b_{bp}
434 and Chl*a* occurs as soon as a DCM takes place, with maximum values of b_{bp} and Chl*a*

encountered in summer when the DCM is the most pronounced, in both the western and eastern Mediterranean basins (Figs. SB1a-e). On the opposite, in the STG regime where durable stratification takes place, DCMs appear as a permanent pattern. The b_{bp} and Chl*a* variations are decoupled and the highest values of both variables are recorded in spring or fall (Figs. SB1f-n).

4 DISCUSSION

The present analysis of a global BGC-Argo database indicates a general power linear relationship between b_{bp} and Chl*a* in the productive layer as well as in the surface and mixed layers. Nevertheless, the analysis of subsets of data suggests a large second-order variability around the global mean relationships, depending on the considered range of values in Chl*a* and b_{bp}, layer of the water column, region or season. In this section, we investigate the sources of variability around the average b_{bp}-to-Chl*a* relationship in our database.

4.1 General relationship between Chl*a* and b_{bp}

The chlorophyll *a* concentration is the most commonly used proxy for the phytoplankton carbon biomass (*Cullen*, 1982; *Siegel et al.*, 2013) whereas the particulate backscattering coefficient is considered as a proxy of the POC in open ocean (*Stramski et al.*, 1999; *Balch et al.*, 2001; *Cetinić et al.*, 2012; *Dall'Olmo and Mork*, 2014) and provides information on the whole pool of particles, not specifically on phototrophic organisms. Over broad biomass gradients, the stock of POC covaries with phytoplankton biomass and hence b_{bp} and Chl*a* show substantial covariation. This is what is observed in the present study when the full database is considered (Fig. 3a). This is also the case when we examine subsets of data from the NSPG and SO regimes, which, although featuring strong seasonality, showing relatively constant relationships between b_{bp} and Chl*a* (Figs. 3a-c, 4a-i and 5a-i). In such environments

458 an increase in the concentration of chlorophyll *a* is associated with an increase in b_{bp}. Such
459 significant relationships between b_{bp} and Chl*a* have indeed been reported in several studies
460 based on relatively large datasets (*Huot et al.*, 2008) or measurements from seasonally
461 dynamic systems (*Stramska et al.*, 2003; *Antoine et al.*, 2011; *Xing et al.*, 2014). Our results
462 corroborate these studies and yield a global relationship of the form $b_{bp}(700) = 0.00181$
463 (± 0.000014) $Chla^{0.605}$ (± 0.00484) for the productive layer.

464 Nevertheless, the b_{bp}-to-Chl*a* relationship is largely variable depending on the considered
465 layer of the water column. Regarding the mixed and surface layers, our study suggests a
466 general relationship with determination coefficients smaller than those calculated for the
467 productive layer. The intercept (~0.0017) and more importantly the slope values (~0.36)
468 associated with the surface layer are also lower than those associated with the productive
469 layer (Table 3); hence for a given level of b_{bp}, the Chl*a* is lower for the surface layer than
470 predicted by the productive layer relationship. Empirical relationships of the literature
471 previously established in various regions in the first few meters of the water column
472 (*Reynolds et al.*, 2001; *Dall'Olmo et al.*, 2009; *Antoine et al.*, 2011; *Xing et al.*, 2014) always
473 show steeper slope compared to our results for the surface layer (Table 2).

Table 3. Empirical relationship obtained between the particulate backscattering coefficient (b_{bp}) and the concentration of chlorophyll *a* (Chl*a*) for the different layers of the water column considered in this study. We also indicate the associated statistics: Root Mean Squared Error (RMSE) and coefficient of determination R^2 for the significance level of $p < 0.001$.

Empirical relationship	Water column layer	R^2	RMSE	Number of data
$b_{bp}(700) = 0.00174\ Chla^{0.360}$	0–Z_{pd}	0.6311	0.000942	5253
$b_{bp}(700) = 0.00171\ Chla^{0.373}$	0–MLD	0.6167	0.000932	8743
$b_{bp}(700) = 0.00147\ Chla^{0.753}$	DCM	0.5667	0.00104	1628
$b_{bp}(700) = 0.00181\ Chla^{0.605}$	0–1.5 Z_{eu}	0.7443	0.000967	5250

To our knowledge, the present study proposes the first analysis of the b_{bp}-to-Chl*a* relationship within the DCM layer. A significant relationship between b_{bp} and Chl*a* is observed and it is associated with the steepest slope, the highest RMSE and the lowest coefficient of determination in comparison with the other layers (Table 3). Thus for the DCM layer, a given level of b_{bp} is associated with higher values of Chl*a* than predicted by the global relationship of the productive layer.

In the next two sections, we will investigate the underlying processes leading to the existence or not of a relationship between b_{bp} and Chl*a* and explore the variability of this relationship along the vertical dimension, the seasons and the distinct bioregions of the different regimes. For this purpose we will consider the behavior of the b_{bp}:Chl*a* ratio with respect to light conditions and phytoplankton community composition.

4.2 Influence of the nature of the particulate assemblage on the b_{bp}-to-Chla relationship

Although the relationship between POC and b_{bp} is evident in some regions, the particulate backscattering coefficient is not a direct proxy of POC. It depends on several parameters such as the concentration of particles in the water column, their size distribution, shape, structure and refractive index (*Morel and Bricaud*, 1986; *Babin and Morel*, 2003; *Huot et al.*, 2007b; *Whitmire et al.*, 2010). The b_{bp} coefficient has been shown to be very sensitive to the presence of picophytoplankton as well as of non-algal particles of the submicron size range (e.g. detritus, bacteria, viruses), especially in oligotrophic waters (*Ahn et al.*, 1992; *Stramski et al.*, 2001; *Vaillancourt et al.*, 2004), but also to particles up to 10 µm (*Loisel et al.*, 2007).

In regions with substantial inputs of mineral particles, a shift towards enhanced b_{bp} values for a constant Chl*a* level occurs (Figs. 4w and x and 5w and x). Substantial concentrations of mineral particles, submicrometer particles of Saharan origin for example, have been shown to cause significant increases in the particulate backscattering signal (*Prospero*, 1996; *Claustre et al.*, 2002; *Stramski et al.*, 2004; *Loisel et al.*, 2011). The EQNASTZ bioregion exhibits, for example, particularly high b_{bp} values compared to the low Chl*a* found in the surface layer (Figs. 4w and 5w). This is not surprising considering that this region is located in the Equatorial North Atlantic dust belt (*Kaufman et al.*, 2005). The Black Sea is also characterized by a higher b_{bp} signal than predicted from Chl*a* based on our global model (Figs. 4x and 5x). This could be explained by the fact that this enclosed sea follows a coastal trophic regime and is strongly influenced by river runoff that may carry small and highly refractive lithogenic particles (*Ludwig et al.*, 2009; *Tanhua et al.*, 2013). Such an increase in backscattering signal may also be related to coccolithophorid blooms (*Balch et al.*, 1996a). These small calcifying microalgae highly backscatter light due to their calcium carbonate

shell and their presence could explain the episodically higher b_{bp} than predicted by the global regression model particularly in the Black Sea where coccolithophorid blooms are frequently reported (*Cokacar et al.*, 2001; *Kopelevich et al.*, 2013) or in the Iceland Basin (*Holligan et al.*, 1993; *Balch et al.*, 1996b) (Fig. 4b or 5b).

Recently, the b_{bp}:Chl*a* ratio, proxy of the POC:Chl*a* ratio (*Behrenfeld et al.*, 2015; *Álvarez et al.*, 2016; *Westberry et al.*, 2016), has been used as an optical index of phytoplankton communities, with low values associated with a dominance of diatoms in the phytoplankton assemblage (*Cetinić et al.*, 2012, 2015). Indeed, in open-ocean waters, phytoplankton generally dominate the pool of particles in the water column. A shift towards higher or weaker b_{bp} values at a constant Chl*a* level may be explained by changes in the phytoplankton community composition. However, in oligotrophic environments, non-algal particles may represent a significant part of the particulate assemblage (*Yentsch and Phinney*, 1989; *Stramski et al.*, 2004; *Loisel et al.*, 2007). Indeed, a background of submicronic living biological cells such as viruses and bacteria or even non-living particles including detritus or inorganic particles could influence the b_{bp}:Chl*a* ratio (e.g. *Morel and Ahn*, 1991; *Claustre et al.*, 1999; *Stramski et al.*, 2001).

The lowest b_{bp}:Chl*a* values in our global database occur in summer in the NSPG and SO regimes (Figs. 6a-i) and are associated with large contributions (>40%) of microphytoplankton to the total Chl*a*. This actually corroborates the hypothesis of *Cetinić et al.* (2012, 2015) that b_{bp}:Chl*a* can be considered as an optical index of the phytoplankton community composition. High values of the b_{bp}:Chl*a* ratio are associated with large contributions of pico- and nanophytoplankton to algal biomass and low values with diatom-dominated communities. The occurrence of microphytoplankton blooms of large-sized phytoplankton community is indeed well-known in the NSPG regime (*Li*, 2002; *Barton et al.*, 2015; *Cetinić et al.*, 2015) or in some productive regions of the Southern Ocean (*Uitz et al.*,

2009; *Georges et al.*, 2014; *Mendes et al.*, 2015). Similarly, in the NW_MED bioregion, low b_{bp}:Chl*a* values are accompanied by large contributions of microphytoplankton during the spring bloom (*Marty and Chiavérini*, 2010; *Siokou-Frangou et al.*, 2010; *Mayot et al.*, 2016). On the opposite, high b_{bp}:Chl*a* values in summer are rather associated with dominant contributions of the pico- and nanophytoplankton to the total chlorophyll biomass (Fig. 6j) and also possibly to higher proportion of non-algal particles, consistently with *Navarro et al.* (2014) or *Sammartino et al.* (2015).

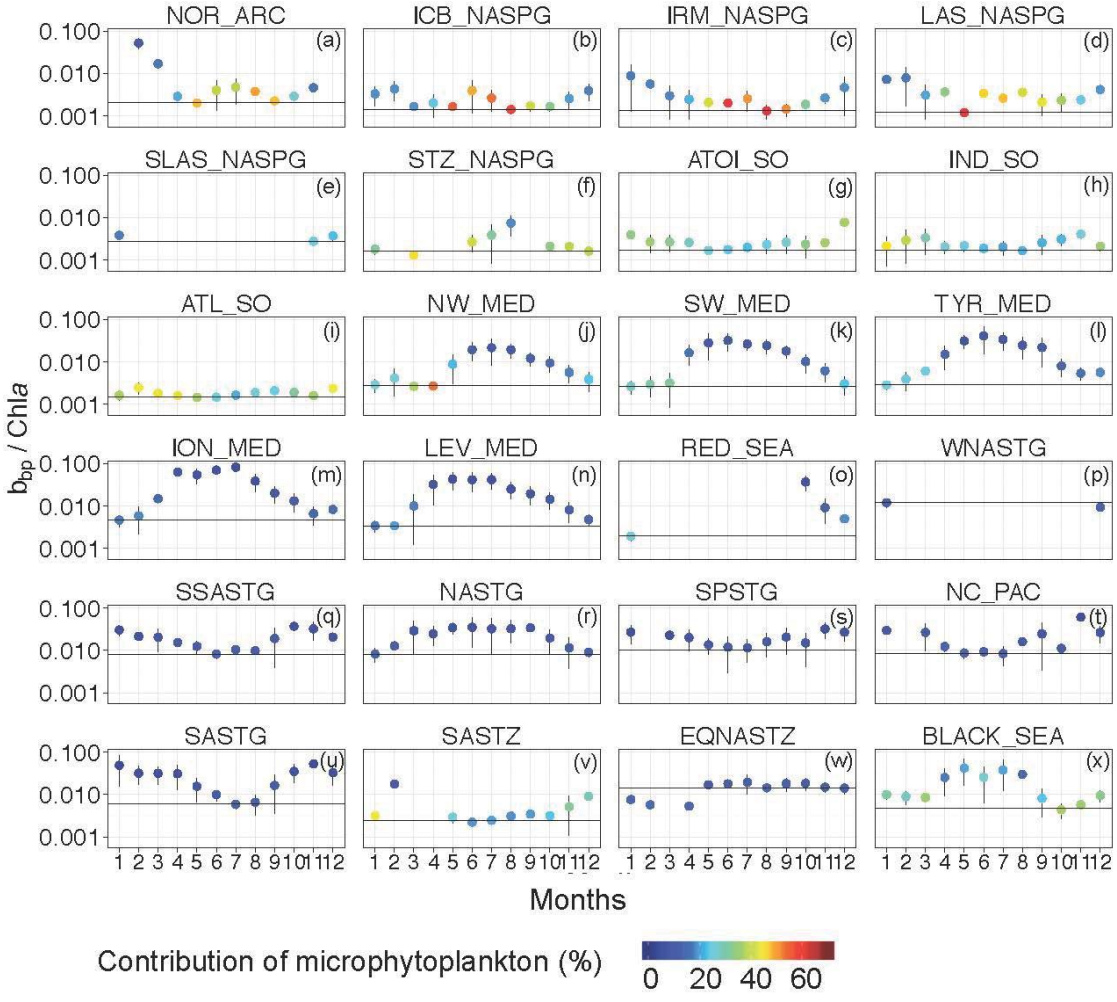

Figure 6: *Monthly climatology of the b_{bp}:Chla ratio within the surface layer (0-Z_{pd}). The color code indicates the fractional contribution of the microphytoplankton to the chlorophyll biomass associated with the entire phytoplankton assemblage, estimated from the Uitz et al. (2006) parameterization. In each panel, the horizontal black line shows the minimum value of the b_{bp}:Chla ratio determined within each bioregion. The black lines represent the standard deviation for each data point.*

In the rest of the Mediterranean basin (SW_MED, TYR_MED and the Eastern Basin) (Figs. 6k-n) as well as in the subtropical regime, the phytoplankton biomass is essentially constant throughout the year with high b_{bp}:Chl*a* values in summer, lower values in winter, and a relatively constant picoplankton-dominated algal community (Figs. 6o-w) (*Dandonneau et al.*, 2004; *Uitz et al.*, 2006; *Ras et al.*, 2008). In this region, the seasonal cycle of the b_{bp}:Chl*a* ratio does not seem to be influenced at a first order by changes in phytoplankton community composition.

4.3 Influence of photoacclimation on the b_{bp}-to-Chla relationship

The Chl*a* is an imperfect proxy of phytoplankton biomass that varies not only with phytoplankton carbon biomass but also with environmental conditions such as light, temperature or nutrient availability (*Cleveland et al.*, 1989; *Babin et al.*, 1996; *Geider et al.*, 1997). Phytoplankton cells adjust their intracellular Chl*a* in response to changes in light conditions through the process of photoacclimation (*Falkowski and Laroche*, 1991; *Lindley et al.*, 1995; *Eisner et al.*, 2003; *Dubinsky and Stambler*, 2009). Photoacclimation-induced variations in intracellular Chl*a* may cause large changes in the Chl*a*-to-carbon ratio (*Geider*, 1987; *Behrenfeld et al.*, 2005; *Sathyendranath et al.*, 2009) and, thus, changes in the b_{bp}-to-Chl*a* ratio (*Behrenfeld and Boss*, 2003; *Siegel et al.*, 2005). In the upper oceanic layer of the water column, photoacclimation to high light may result in an increase in the b_{bp}-to-Chl*a* ratio whereas a decrease in this ratio occurs in DCM layers or in the upper layer during winter time in subpolar regimes (NSPG and SO) where photoacclimation to low light occurs.

The impact of light conditions on the b_{bp}:Chl*a* ratio in the different regimes is illustrated in Fig. 8. Significant trends are observed in the different layers of the water column for all regimes except for the Black Sea. In the NSPG and SO regimes, the b_{bp}:Chl*a* ratio remains relatively constant with respect to the normalized PAR regardless of the considered layer of

573 the water column (Figs. 7a-c). In contrast, the Mediterranean Sea and the subtropical gyres
574 show a decoupling between b_{bp} and Chl*a* (Fig. 5k-w) so the b_{bp}:Chl*a* ratio in the productive,
575 mixed or surface layer increases with an increase in the normalized PAR (Fig. 7a-c). The
576 seasonal cycle of the b_{bp}:Chl*a* ratio in these regimes results from variations in Chl*a* whereas
577 b_{bp} remains relatively constant over the seasons (not shown). Thus, our results suggest that the
578 variability in the b_{bp}:Chla ratio in the NSPG and SO regimes is not driven at first order by
579 phytoplankton acclimation to light level even if such a process is known to occur at shorter
580 temporal and spatial scales in those regimes (*Lutz et al.*, 2003; *Behrenfeld et al.*, 2015). On
581 the opposite, in both the MED and STG regimes the b_{bp}:Chla ratio variations are essentially
582 driven by phytoplankton photoacclimation.

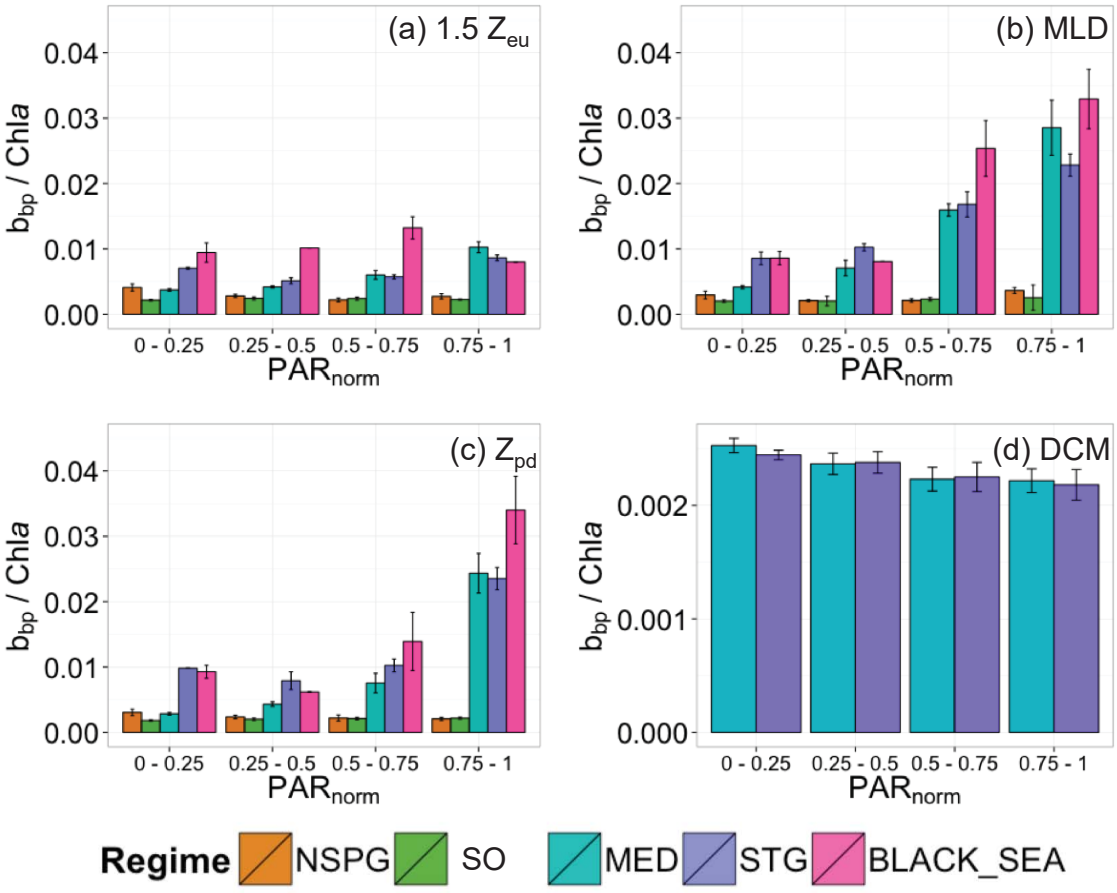

583 **Figure 7**: *Histogram of the monthly median b_{bp}:Chla ratio as a function of the normalized*
584 *Photosynthetically Available Radiation (PAR_{norm}) for each regime within (a) the layer*
585 *comprised between the surface and 1.5 Z_{eu}; (b) the mixed layer; (c) the surface layer; and (d)*

within the DCM layer. The color code indicates the regimes in which the BGC-Argo data were collected. Note the different y-scale for panel (d) compared to panels (a), (b) and (c). The black lines on the top of each bar represent the standard deviation.

In these oligotrophic regimes, Chl*a* within the DCM layer is at least a factor of 2 higher than in the productive layer (Fig. 6). In the lower part of the euphotic zone, phytoplankton cells hence adjust their intracellular Chl*a* to low light conditions, resulting in a decrease in the b_{bp}:Chl*a* ratio. In addition, the b_{bp}:Chl*a* ratio in this layer seems to remain constant within a regime regardless of absolute light conditions (Fig. 7d). Actually, the absolute values of PAR essentially vary between 10 and 25 µmol quanta m^{-2} s^{-1} in all the bioregions along the year with values exceeding 50 µmol quanta m^{-2} s^{-1} only in the NW_MED and EQNASTZ bioregions. As reported by *Letelier et al.* (2004) and *Mignot et al.* (2014), the DCM may follow a given isolume along the seasonal cycle and is thus essentially light-driven. Finally, we suggest that the relative homogeneity of both the environmental (PAR) conditions and phytoplankton community composition at the DCM level in subtropical regimes may explain the relative stability of the b_{bp}:Chl*a* values in this water column layer. In the Mediterranean Sea, in contrast, some studies evoke changes in phytoplankton communities in the DCM layer (*Crombet et al.*, 2011) suggesting our results might be further explored when relevant data are available.

4.4 Variability in the b_{bp}-to-Chla relationship is driven by a combination of factors

In the previous sections, we examined the processes that potentially drive the variability in the b_{bp}-to-Chl*a* relationship in the various oceanic regimes considered here.

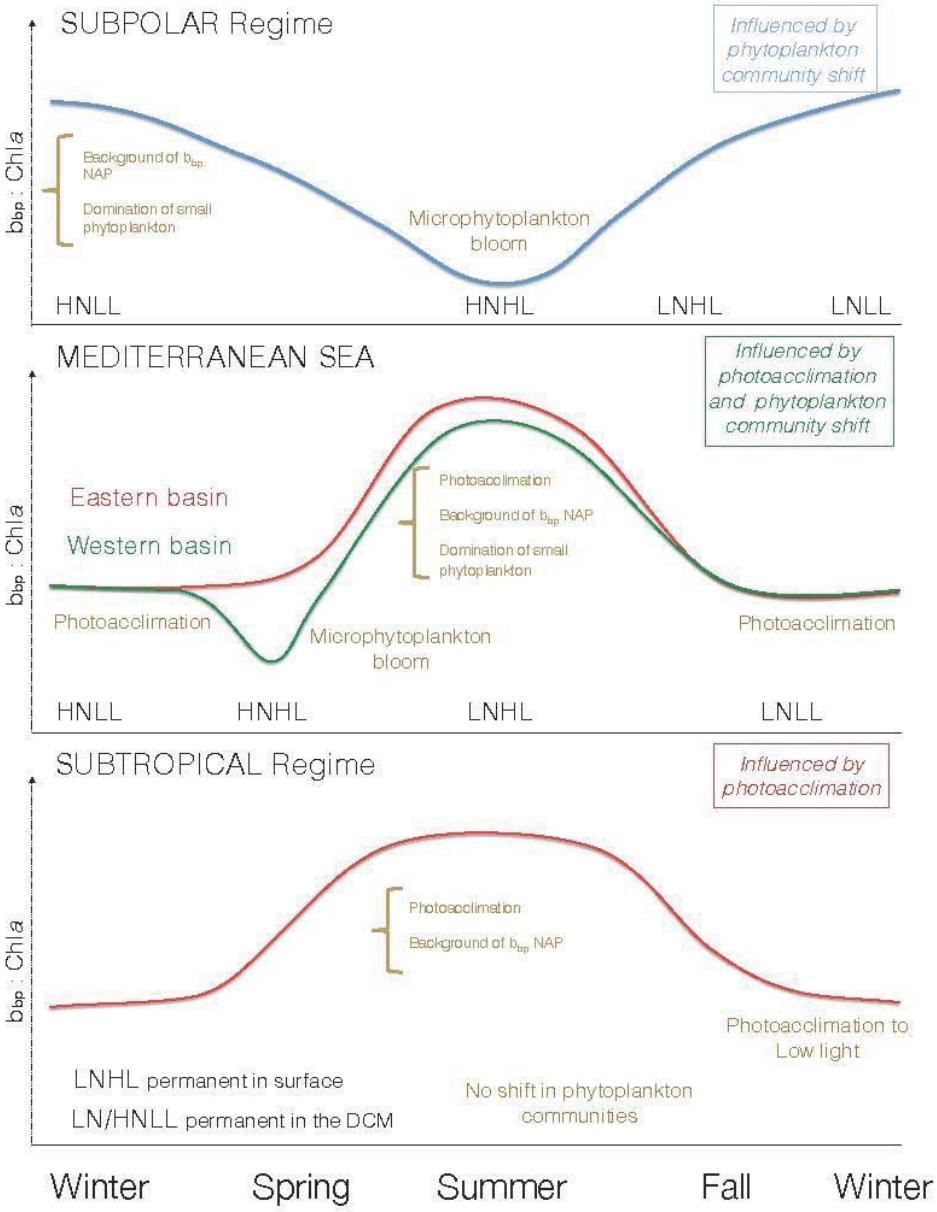

609

610 **Figure 8**: *Conceptual scheme of the seasonal cycle of the b_{bp}:Chla ratio in the surface layer*
611 *of the ocean with potential factors explaining its variability. HNLL: High Nutrient Low Light;*
612 *HNHL: High Nutrient High Light; LNHL: Low Nutrient High Light; LNLL: Low Nutrient*
613 *Low Light.*

614

In the subpolar regimes NSPG and SO, changes in the composition of the particle assemblage, phytoplankton communities in particular, are likely the first-order driver of the seasonal variability in the b_{bp}-to-Chl*a* ratio (Fig. 8). In these regimes, the b_{bp}:Chl*a* ratio remains constant regardless of the light intensity in both the productive and surface layers suggesting that phytoplankton photoacclimation is likely not an important driver of the variability in the b_{bp}-to-Chl*a* relationship. We note, however, that in the SO other factors may come into play, such as the light-mixing regime or iron-limitation (e.g. *Boyd*, 2002; *Blain et al.*, 2007, 2013). On the opposite, in the subtropical regime, Chl*a* and b_{bp} are decoupled in the surface layer as well as in the DCM layer. Thus, photoacclimation seems to be the main process driving the vertical and seasonal variability of the b_{bp}-to-Chl*a* relationship, although a varying contribution of non-algal particles to the particle pool cannot be excluded.

Whereas the subpolar and the subtropical regimes behave as a "biomass regime" and a "photoacclimation regime" (sensu *Siegel et al.*, 2005), respectively, the Mediterranean Sea stands as an intermediate regime between these two end-members. The large number of data available in the Mediterranean allows us to describe this intermediate situation (Fig. 8). The Mediterranean Sea appears as a more complex and variable system than the stable and resilient subtropical gyres. Along with the ongoing development of the global Bio-Argo program and associated float deployments, additional data collected in underrepresented regions will become available to make our database more robust and will help to improve our analysis. Indeed, in the surface layer of the Mediterranean system, a high b_{bp}:Chl*a* ratio in summer has previously been attributed not only to (i) a background of submicronic living biological cells such as viruses and bacteria or large contribution of non-living particles including detritus or inorganic particles (*Claustre et al.*, 1999; *Bricaud et al.*, 2004; *Oubelkheir et al.*, 2005), or to (ii) photoacclimation of phytoplankton cells to high light conditions as suggested by *Bellacicco et al.* (2016), but also to (iii) a shift towards small

phytoplankton dominated communities (pico- or nanophytoplankton) after the seasonal microphytoplankton bloom.

Following the longitudinal trophic gradient of the Mediterranean Sea, we observe a variation in the biogeochemical status of the DCM (Fig. A1a-d). The DCM may be attributed to low light photoacclimation similarly to the DCM observed in the STG regime. Yet, under favorable light and nutrient conditions encountered in the Western Mediterranean basin, the DCM could result from a real biomass increase occurring at depth instead of a simple photoacclimation "artifact" (*Winn et al.*, 1995; *Beckmann and Hense*, 2007; *Cullen*, 2014; *Mignot et al.*, 2014). In such conditions referred to as "Deep Biomass Maximum" (DBM), a concurrent increase in Chl*a* and POC associated with large phytoplankton cells leads to constantly low values of the b_{bp}:Chl*a* ratio (Fig. 7d). Our results corroborate previous studies (*Latasa et al.*, 1992; *Crombet et al.*, 2011; *Mignot et al.*, 2014) about the seasonal occurrence of a DBM in the western basin of Mediterranean sea. This deep feature could actually represent a significant source of phytoplankton carbon biomass that is ignored by satellite ocean color sensors that only probe the surface layer of the water column.

5 CONCLUSIONS

The main goal of the present study was to examine the variability of the relationship between the particulate backscattering coefficient and the chlorophyll *a* concentration over a broad range of oceanic conditions. Using an extensive BGC-Argo profiling float database, we investigated the sources of variability in this relationship with respect to the vertical dimension as well as on a seasonal and regional scale. In accordance with previous studies (*Reynolds et al.*, 2001; *Stramska et al.*, 2003; *Huot et al.*, 2008; *Dall'Olmo et al.*, 2009; *Antoine et al.*, 2011; *Xing et al.*, 2014) and consistently with the so-called "bio-optical assumption" (*Smith and Baker*, 1978b; *Siegel et al.*, 2005), a general covariation between b_{bp}

and Chl*a* is observed at a global scale (*Loisel and Morel*, 1998) in the productive layer of the water column (0-1.5 Z_{eu}). Although this covariation seems to be permanent in subpolar regimes in relation with large-amplitude phytoplankton biomass seasonal cycles (*Henson et al.*, 2006; *Boss and Behrenfeld*, 2010; *Lacour et al.*, 2015), several nuances have been revealed according to the season, considered layer of the water column and bioregion. We suggest that the b_{bp}:Chl*a* ratio, proxy of the C:Chl*a* ratio (*Behrenfeld et al.*, 2015; *Westberry et al.*, 2016), can be used as an index of the nature (composition and size) of the particle assemblage in a "biomass regime" (NSPG and SO regimes and Western Mediterranean basin) or as a photophysiological index in a "photoacclimation regime" (STG regime and Eastern Mediterranean basin).

The present analysis provides insights into the coupling between major proxies of the POC and phytoplankton biomass in key regimes encountered in the world's open oceans. It points to the strong potential of the recently available global BGC-Argo float database to address regional or seasonal nuances in first order relationships that have been established in the past on admittedly restricted datasets. In addition, this study stresses out the large variability in the b_{bp}-to-Chl*a* relationship, which is critical to the bio-optical modeling of the b_{bp} coefficient in several semi-empirical ocean color models (*Garver and Siegel*, 1997; *Lee et al.*, 2002; *Maritorena et al.*, 2002). Indeed, bio-optical and reflectance models require detailed knowledge and parameterization of the average trends in the inherent optical properties, especially in open-ocean waters where these trends can be related to Chl*a*. Although the analysis of the impact of such variability on ocean color modeling is out of the scope of the present paper, we expect our analysis to be potentially useful in the context of applications to ocean color. Finally, as the amount of BGC-float data will continue to increase, it will be possible to reassess the variability of bio-optical relationships and to establish new "global" standards and regional parameterizations.

ACKNOWLEDGEMENTS

This paper represents a contribution to the following research projects: remOcean (funded by the European Research Council, Grant Agreement No 246777), NAOS (funded by the Agence Nationale de la Recherche in the frame of the French ‘‘Equipement d’avenir’’ program, Grant Agreement No ANR J11R107-F), AtlantOS (funded by the European Union’s Horizon 2020 research and innovation program, Grant Agreement No 2014-633211), E-AIMS (funded by the European Commission’s FP7 project, Grant Agreement No 312642), U.K. Bio-Argo (funded by the British Natural Environment Research Council – NERC, Grant Agreement No NE/L012855/1), REOPTIMIZE (funded by the European Union’s Horizon 2020 research and innovation program, Marie Skłodowska-Curie Grant Agreement No 706781), Argo-Italy (funded by the Italian Ministry of Education, University and Research - MIUR), and the French Bio-Argo program (Bio-Argo France; funded by CNES-TOSCA, LEFE Cyber, and GMMC). We thank the PIs of several BGC-Argo floats missions and projects: Giorgio Dall’Olmo (Plymouth Marine Laboratory, United Kingdom; E-AIMS and U.K. Bio-Argo); Kjell-Arne Mork (Institute of Marine Research, Norway; E-AIMS); Violeta Slabakova (Bulgarian Academy of Sciences, Bulgaria; E-AIMS); Emil Stanev (University of Oldenburg, Germany; E-AIMS); Claire Lo Monaco (Laboratoire d’Océanographie et du Climat: Expérimentations et Approches Numériques); Pierre-Marie Poulain (National Institute of Oceanography and Experimental Geophysics, Italy; Argo-Italy); Sabrina Speich (Laboratoire de Météorologie Dynamique, France; LEFE-GMMC); Virginie Thierry (Ifremer, France; LEFE-GMMC); Pascal Conan (Observatoire Océanologique de Banyuls sur mer, France; LEFE-GMMC); Laurent Coppola (Laboratoire d’Océanographie de Villefranche, France; LEFE-GMMC); Anne Petrenko (Mediterranean Institute of Oceanography, France; LEFE-GMMC); and Jean-Baptiste Sallée (Laboratoire d’Océanographie et du Climat, France; LEFE-GMMC). Collin Roesler (Bowdoin College, USA) and Yannick Huot (University of

Sherbrooke, Canada) are acknowledged for useful comments and fruitful discussion. We also thank the International Argo Program and the CORIOLIS project that contribute to make the data freely and publicly available. Data referring to (*Organelli et al.*, 2016a) (doi:10.17882/47142) and (*Barbieux et al.,* 2017) (doi: 10.17882/49388) are freely available on SEANOE.

REFERENCES

Ahn, Y.-H., A. Bricaud, and A. Morel (1992), Light backscattering efficiency and related properties of some phytoplankters, *Deep. Res.*, *39*(11), 1835–1855.

Álvarez, E., X. A. G. Morán, Á. López-Urrutia, and E. Nogueira (2016), Size-dependent photoacclimation of the phytoplankton community in temperate shelf waters (southern Bay of Biscay), *Mar. Ecol. Prog. Ser.*, *543*, 73–87, doi:10.3354/meps11580.

Antoine, D., D. A. Siegel, T. Kostadinov, S. Maritorena, N. B. Nelson, B. Gentili, V. Vellucci, and N. Guillocheau (2011), Variability in optical particle backscattering in contrasting bio-optical oceanic regimes, *Limnol. Oceanogr.*, *56*(3), 955–973, doi:10.4319/lo.2011.56.3.0955.

Babin, M., and A. Morel (2003), Light scattering properties of marine particles in coastal and open ocean waters as related to the particle mass concentration, *Limnol. Oceanogr.*, *48*(2), 843–859, doi:10.4319/lo.2003.48.2.0843.

Babin, M., A. Morel, and B. Gentili (1996), Remote sensing of sea surface Sun-induced chlorophyll fluorescence: consequences of natural variations in the optical characteristics of phytoplankton and the quantum yield of chlorophyll a fluorescence, *Int. J. Remote Sens.*, *17*(12), 2417–2448.

Balch, W. M., K. a. Kilpatrick, P. Holligan, D. Harbour, and E. Fernandez (1996a), The 1991 coccolithophore bloom in the central North Atlantic. 2. Relating optics to coccolith concentration, *Limnol. Oceanogr.*, *41*(8), 1684–1696, doi:10.4319/lo.1996.41.8.1684.

Balch, W. M., K. A. Kilpatrick, and C. C. Trees (1996b), The 1991 coccolithorphore bloom in the central North Atlantic: I. Optical properties and factors affecting their distribution., *Limnol. Oceanogr.*, *41*(8), 1669–1683.

Balch, W. M., D. T. Drapeau, J. J. Fritz, B. C. Bowler, and J. Nolan (2001), Optical backscattering in the Arabian Sea—continuous underway measurements of particulate inorganic and organic carbon, *Deep Sea Res. I*, *48*(11), 2423–2452, doi:10.1016/S0967-0637(01)00025-5.

Barbieux, M. et al. (2017), A global database of vertical profiles derived from Biogeochemical Argo float measurements for

biogeochemical and bio-optical applications, *SEANOE*, doi:doi:10.17882/49388.

Barton, A. D., M. S. Lozier, and R. G. Williams (2015), Physical controls of variability in North Atlantic phytoplankton communities, *Limnol. Oceanogr.*, *60*(1), 181–197, doi:10.1002/lno.10011.

Beckmann, A., and I. Hense (2007), Beneath the surface: Characteristics of oceanic ecosystems under weak mixing conditions - A theoretical investigation, *Prog. Oceanogr.*, *75*(4), 771–796, doi:10.1016/j.pocean.2007.09.002.

Behrenfeld, M. J., and E. Boss (2003), The beam attenuation to chlorophyll ratio: an optical index of phytoplankton physiology in the surface ocean ?, *Deep Sea Res. I*, *50*(12), 1537–1549, doi:10.1016/j.dsr.2003.09.002.

Behrenfeld, M. J., E. Boss, D. A. Siegel, and D. M. Shea (2005), Carbon-based ocean productivity and phytoplankton physiology from space, *Global Biogeochem. Cycles*, *19*(1), 1–14, doi:10.1029/2004GB002299.

Behrenfeld, M. J., R. T. O'Malley, E. S. Boss, T. K. Westberry, J. R. Graff, K. H. Halsey, A. J. Milligan, D. A. Siegel, and M. B. Brown (2015), Revaluating ocean warming impacts on global phytoplankton, *Nat. Clim. Chang.*, *6*(3), 323–330, doi:10.1038/nclimate2838.

Bellacicco, M., G. Volpe, S. Colella, and R. Santoleri (2016), Role of photoacclimation on phytoplankton's seasonal cycle in the Mediterranean Sea through satellite ocean color data, *Remote Sens. Environ.*, *184*, 595–604, doi:10.1016/j.rse.2016.08.004.

Biogeochemical-Argo Planning Group (2016), The scientific rationale, design, and implementation plan for a Biogeochemical-Argo float array, *Ed. by K. Johnson H. Claustre*, doi:10.13155/46601.

Birge, R. T. (1939), The Propagation of Errors, *Am. J. Phys.*, *7*(6), 351–357, doi:10.1119/1.1991484.

Bishop, J. K. B. (2009), Autonomous observations of the ocean biological carbon pump, *Oceanography*, *24*(3), 162–173, doi:10.5670/oceanog.2011.65.

Blain, S. et al. (2007), Effect of natural iron fertilization on carbon sequestration in the Southern Ocean, *Nature*, *446*(7139), 1070–1074, doi:10.1038/nature05700.

Blain, S., S. Renaut, X. Xing, H. Claustre, and C. Guinet (2013), Instrumented elephant seals reveal the seasonality in chlorophyll and light-mixing regime in the iron-fertilized Southern Ocean, *Geophys. Res. Lett.*, *40*(24), 6368–6372, doi:10.1002/2013GL058065.

Boss, E., and M. Behrenfeld (2010), In situ evaluation of the initiation of the North Atlantic phytoplankton bloom, *Geophys. Res. Lett.*, *37*(18), 1–5, doi:10.1029/2010GL044174.

Boss, E., and W. S. Pegau (2001), Relationship of light scattering at an angle in the backward direction to the backscattering coefficient, *Appl. Opt.*, *40*(30), 5503–5507, doi:10.1364/AO.40.005503.

Boyd, P. W. (2002), Environmental factors controlling phytoplankton processes in the Southern Ocean, *J. Phycol.*, *38*(5),

844–861, doi:10.1046/j.1529-8817.2002.t01-1-01203.x.

de Boyer Montégut, C. (2004), Mixed layer depth over the global ocean: An examination of profile data and a profile-based climatology, *J. Geophys. Res.*, *109*, 1–20, doi:10.1029/2004JC002378.

Brainerd, K. E., and M. C. Gregg (1995), Surface mixed and mixing layer depths, *Deep Sea Res. I*, *42*(9), 1521–1543.

Bricaud, A., C. Roesler, and J. R. V. Zaneveld (1995), In situ methods for measuring the inherent optical properties of ocean waters, *Limnol. Oceanogr.*, *40*(2), 393–410, doi:10.4319/lo.1995.40.2.0393.

Bricaud, A., H. Claustre, J. Ras, and K. Oubelkheir (2004), Natural variability of phytoplanktonic absorption in oceanic waters: Influence of the size structure of algal populations, *J. Geophys. Res.*, *109*(C11), doi:10.1029/2004JC002419.

Briggs, N., M. J. Perry, I. Cetinić, C. Lee, E. D'Asaro, A. M. Gray, and E. Rehm (2011), High-resolution observations of aggregate flux during a sub-polar North Atlantic spring bloom, *Deep Sea Res. I*, *58*(10), 1031–1039, doi:10.1016/j.dsr.2011.07.007.

Brown, C. A., Y. Huot, P. J. Werdell, B. Gentili, and H. Claustre (2008), The origin and global distribution of second order variability in satellite ocean color and its potential applications to algorithm development, *Remote Sens. Environ.*, *112*(12), 4186–4203, doi:10.1016/j.rse.2008.06.008.

Cetinić, I., M. J. Perry, N. T. Briggs, E. Kallin, E. A. D'Asaro, and C. M. Lee (2012), Particulate organic carbon and inherent optical properties during 2008 North Atlantic Bloom Experiment, *J. Geophys. Res.*, *117*, C06028, doi:10.1029/2011JC007771.

Cetinić, I., M. J. Perry, E. D'Asaro, N. Briggs, N. Poulton, M. E. Sieracki, and C. M. Lee (2014), Optical community index to assess spatial patchiness during the 2008 North Atlantic Bloom, *Biogeosciences Discuss.*, *11*(9), 12833–12870, doi:10.5194/bgd-11-12833-2014.

Cetinić, I., M. J. Perry, E. D'Asaro, N. Briggs, N. Poulton, M. E. Sieracki, and C. M. Lee (2015), A simple optical index shows spatial and temporal heterogeneity in phytoplankton community composition during the 2008 North Atlantic Bloom Experiment, *Biogeosciences*, *12*(7), 2179–2194, doi:10.5194/bg-12-2179-2015.

Claustre, H., A. Morel, M. Babin, C. Cailliau, D. Marie, J.-C. Marty, D. Tailliez, and D. Vaulot (1999), Variability in particle attenuation and chlorophyll fluorescence in the tropical Pacific : Scales, patterns, and biogeochemical implications, *J. Geophys. Res.*, *104*(C2), 3401–3422.

Claustre, H., A. Morel, S. B. Hooker, M. Babin, D. Antoine, K. Oubelkheir, A. Bricaud, K. Leblanc, B. Quéguiner, and S. Maritorena (2002), Is desert dust making oligotrophic waters greener?, *Geophys. Res. Lett.*, *29*(10), 107-1-107–4, doi:10.1029/2001GL014056.

Claustre, H. et al. (2010), Bio-optical profiling floats as new observational tools for biogeochemical and ecosystem studies:

802 Potential synergies with ocean color remote sensing., in *"Proceedings of the OceanObs'09: Sustained Ocean*
803 *Observations and Information for Society" Conference*, edited by J. Hall, D. E. Harrison, and D. Stammer, ESA Publ.
804 WPP-306, Venice, Italy, 21–25 Sep.

805 Cleveland, J. S., M. J. Perry, D. A. Kiefer, and M. C. Talbot (1989), Maximal quantum yield of photosynthesis in the
806 northwest Sargasso Sea., *J. Mar. Res.*, *47*, 869–886.

807 Cokacar, T., N. Kubilay, and T. Oguz (2001), Structure of Emiliania huxleyi blooms in the Black Sea surface waters as
808 detected by SeaWIFS imagery, *Geophys. Res. Lett.*, *28*(24), 4607–4610, doi:10.1029/2001GL013770.

809 Crombet, Y., K. Leblanc, B. Quéuiner, T. Moutin, P. Rimmelin, J. Ras, H. Claustre, N. Leblond, L. Oriol, and M. Pujo-Pay
810 (2011), Deep silicon maxima in the stratified oligotrophic Mediterranean Sea, *Biogeosciences*, *8*(2), 459–475,
811 doi:10.5194/bg-8-459-2011.

812 Cullen, J. J. (1982), The Deep Chlorophyll Maximum : Comparing Vertical Profiles of Chlorophyll a, *Can. J. Fish.Aquat.Sci*,
813 *39*, 791–803.

814 Cullen, J. J. (2014), Subsurface Chlorophyll Maximum Layers: Enduring Enigma or Mystery Solved ?, *Ann. Rev. Mar. Sci.*,
815 *7*, 207–239, doi:10.1146/annurev-marine-010213-135111.

816 Dall'Olmo, G., and K. A. Mork (2014), Carbon export by small particles in the Norwegian Sea, *Geophys. Res. Lett.*, *41*(8),
817 2921–2927, doi:10.1002/2014GL059244.

818 Dall'Olmo, G., T. K. Westberry, M. J. Behrenfeld, E. Boss, and W. H. Slade (2009), Significant contribution of large
819 particles to optical backscattering in the open ocean, *Biogeosciences*, *6*(6), 947–967, doi:10.5194/bg-6-947-2009.

820 Dandonneau, Y., P.-Y. Deschamps, J.-M. Nicolas, H. Loisel, J. Blanchot, Y. Montel, F. Thieuleux, and G. Bécu (2004),
821 Seasonal and interannual variability of ocean color and composition of phytoplankton communities in the North
822 Atlantic, equatorial Pacific and South Pacific, *Deep Sea Res. II*, *51*(1–3), 303–318, doi:10.1016/j.dsr2.2003.07.018.

823 Dickey, T. D. (2003), Emerging ocean observations for interdisciplinary data assimilation systems, *J. Mar. Syst.*, *40–41*, 5–
824 48, doi:10.1016/S0924-7963(03)00011-3.

825 Dubinsky, Z., and N. Stambler (2009), Photoacclimation processes in phytoplankton: Mechanisms, consequences, and
826 applications, *Aquat. Microb. Ecol.*, *56*(2–3), 163–176, doi:10.3354/ame01345.

827 Eisner, L. B., M. S. Twardowski, T. J. Cowles, and M. J. Perry (2003), Resolving phytoplankton photoprotective :
828 photosynthetic carotenoid ratios on fine scales using in situ spectral absorption measurements, *Limnol. Oceanogr.*,
829 *48*(2), 632–646, doi:10.4319/lo.2003.48.2.0632.

830 Falkowski, P. G., and J. Laroche (1991), Acclimation to spectral irradiance in algae, *J. Phycol.*, *27*, 8–14, doi:10.1111/j.0022-
831 3646.1991.00008.x.

832 Flory, E. N., P. S. Hill, T. G. Milligan, and J. Grant (2004), The relationship between floc area and backscatter during a
833 spring phytoplankton bloom, *Deep Sea Res. I*, *51*(2), 213–223, doi:10.1016/j.dsr.2003.09.012.

834 Gardner, W. D., A. V. Mishonov, and M. J. Richardson (2006), Global POC concentrations from in-situ and satellite data,
835 *Deep. Res. II*, *53*(5–7), 718–740, doi:10.1016/j.dsr2.2006.01.029.

836 Garver, S. A., and D. A. Siegel (1997), Inherent optical property inversion of ocean color spectra and its biogeochemical
837 interpretation 1. Time series from the Sargasso Sea, *J. Geophys. Res.*, *102*(96), 607–625.

838 Geider, R. J. (1987), Light and temperature dependence of the carbon to chlorophyll a ratio in microalgae and cyanobacteria :
839 Implications for physiology and growth of phytoplankton, *New Phytol.*, *106*(1), 1–34.

840 Geider, R. J. (1993), Quantitative phytoplankton physiology: implications for primary production and phytoplankton growth,
841 *ICES Mar. Sci. Symp.*, *197*, 52–62.

842 Geider, R. J., H. L. MacIntyre, and T. M. Kana (1997), Dynamic model of phytoplankton growth and acclimation: Responses
843 of the balanced growth rate and the chlorophyll a:carbon ratio to light, nutrient-limitation and temperature, *Mar. Ecol.*
844 *Prog. Ser.*, *148*(1–3), 187–200, doi:10.3354/meps148187.

845 Georges, C., S. Monchy, S. Genitsaris, and U. Christaki (2014), Protist community composition during early phytoplankton
846 blooms in the naturally iron-fertilized Kerguelen area (Southern Ocean), *Biogeosciences*, *11*(20), 5847–5863,
847 doi:10.5194/bg-11-5847-2014.

848 Gordon, H. R., and W. R. McCluney (1975), Estimation of the Depth of Sunlight Penetration in the Sea for Remote Sensing,
849 *Appl. Opt.*, *14*(2), 413–416, doi:10.1364/AO.14.000413.

850 Gordon, R., O. B. Brown, H. Evans, W. Brown, C. Smith, K. Baker, and D. K. Clark (1988), A Semianalytic Radiance
851 Model of Ocean Color, *J. Geophys. Res.*, *93*(8), 10909–10924.

852 Graff, J. R., A. J. Milligan, and M. J. Behrenfeld (2012), The measurement of phytoplankton biomass using flow-cytometric
853 sorting and elemental analysis of carbon, *Limnol. Oceanogr. Methods*, *10*, 910–920, doi:10.4319/lom.2012.10.910.

854 Graff, J. R., T. K. Westberry, A. J. Milligan, M. B. Brown, G. Dall'Olmo, V. Van Dongen-Vogels, K. M. Reifel, and M. J.
855 Behrenfeld (2015), Analytical phytoplankton carbon measurements spanning diverse ecosystems, *Deep Sea Res. I*,
856 *102*, 16–25, doi:10.1016/j.dsr.2015.04.006.

857 Halsey, K. H., and B. M. Jones (2015), Phytoplankton Strategies for Photosynthetic Energy Allocation, *Ann. Rev. Mar. Sci.*,
858 *7*(1), 265–297, doi:10.1146/annurev-marine-010814-015813.

859 Henson, S. a., I. Robinson, J. T. Allen, and J. J. Waniek (2006), Effect of meteorological conditions on interannual variability
860 in timing and magnitude of the spring bloom in the Irminger Basin, North Atlantic, *Deep Sea Res. I*, *53*(10), 1601–
861 1615, doi:10.1016/j.dsr.2006.07.009.

862 Holligan, P. M. et al. (1993), A biogeochemical study of the coccolithophore, Emiliania huxleyi, in the north atlantic, *Global*
863 *Biogeochem. Cycles*, *7*(4), 879–900.

864 Honjo, S. et al. (2014), Understanding the role of the biological pump in the global carbon cycle: An imperative for ocean
865 science, *Oceanography*, *27*(3), 10–16, doi:10.5670/oceanog.2014.78.

866 Huot, Y., and D. Antoine (2016), Remote sensing reflectance anomalies in the ocean, *Remote Sens. Environ.*, *184*, 101–111,
867 doi:10.1016/j.rse.2016.06.002.

868 Huot, Y., M. Babin, F. Bruyant, C. Grob, M. S. Twardowski, H. Claustre, and C. To (2007), Relationship between
869 photosynthetic parameters and different proxies of phytoplankton biomass in the subtropical ocean, *Biogeosciences*, *4*,
870 853–868, doi:10.5194/bg-4-853-2007.

871 Huot, Y., A. Morel, M. S. Twardowski, D. Stramski, and R. A. Reynolds (2008), Particle optical backscattering along a
872 chlorophyll gradient in the upper layer of the eastern South Pacific Ocean, *Biogeosciences*, *5*, 495–507,
873 doi:10.5194/bgd-4-4571-2007.

874 IOCCG (2006), Remote Sensing of Inherent Optical Properties : Fundamentals, Tests of Algorithms, and Applications,
875 *IOCCG Rep. Ser. 5*, 1–126, doi:10.1006/jmbi.1998.2073.

876 IOCCG (2011), Bio-Optical Sensors on Argo Floats, *IOCCG Rep. Ser. 11*, 1–89.

877 Johnson, K., and H. Claustre (2016), Bringing Biogeochemistry into the Argo Age, *Eos (Washington. DC).*, 1–7,
878 doi:10.1029/2016EO062427.

879 Kaufman, Y. J., I. Koren, L. A. Remer, D. Tanré, P. Ginoux, and S. Fan (2005), Dust transport and deposition observed from
880 the Terra-Moderate Resolution Imaging Spectroradiometer (MODIS) spacecraft over the Atlantic Ocean, *J. Geophys.*
881 *Res.*, *110*(10), 1–16, doi:10.1029/2003JD004436.

882 Kiefer, D. A., S. Diego, and L. Jolla (1973), Chlorophyll a Fluorescence in Marine Centric Diatoms: Responses of
883 Chloroplasts to Light and Nutrient Stress, *Mar. Biol.*, *46*, 39–46.

884 Kopelevich, O., V. Burenkov, S. Sheberstov, S. Vazyulya, M. Kravchishina, L. Pautova, V. Silkin, V. Artemiev, and A.
885 Grigoriev (2013), Satellite monitoring of coccolithophore blooms in the Black Sea from ocean color data, *Remote*
886 *Sens. Environ.*, *146*, 113–123, doi:10.1016/j.rse.2013.09.009.

887 Ku, H. H. (1966), Notes on the use of propagation of error formulas, *J. Res. Natl. Bur. Stand. Sect. C Eng. Instrum.*, *70C*(4),
888 263, doi:10.6028/jres.070C.025.

889 Lacour, L., H. Claustre, L. Prieur, and F. D. Ortenzio (2015), Phytoplankton biomass cycles in the North Atlantic subpolar
890 gyre: A similar mechanism for two different blooms in the Labrador Sea, *Geophys. Res. Lett.*, *42*(13), 5403–5410,
891 doi:10.1002/2015GL064540.

892 Latasa, M., M. Estrada, and M. Delgado (1992), Plankton pigment relationships in the Northwestern Mediterranean during
893 stratification, *Mar. Ecol. Prog. Ser.*, *88*, 61–73.

894 Lee, Z., K. L. Carder, and R. a Arnone (2002), Deriving inherent optical properties from water color: a multiband quasi-
895 analytical algorithm for optically deep waters., *Appl. Opt.*, *41*(27), 5755–72, doi:10.1364/AO.41.005755.

896 Legendre, L., R. B. Rivkin, M. G. Weinbauer, L. Guidi, and J. Uitz (2015), The microbial carbon pump concept: Potential
897 biogeochemical significance in the globally changing ocean, *Prog. Oceanogr.*, *134*, 432–450,
898 doi:10.1016/j.pocean.2015.01.008.

899 Letelier, R. M., D. M. Karl, M. R. Abbott, and R. R. Bidigare (2004), Light driven seasonal patterns of chlorophyll and
900 nitrate in the lower euphotic zone of the North Pacific Subtropical Gyre, *Limnol. Oceanogr.*, *49*(2), 508–519,
901 doi:10.4319/lo.2004.49.2.0508.

902 Lewis, M. R., J. J. Cullen, and T. Platt (1983), Phytoplankton and thermal structure in the upper ocean: Consequences of
903 nonuniformity in chlorophyll profile, *J. Geophys. Res.*, *88*(C4), 2565–2570, doi:10.1029/JC088iC04p02565.

904 Li, W. K. W. (2002), Macroecological patterns of phytoplankton in th northwestern North Atlantic Ocean, *Nature*,
905 *419*(6903), 154–157, doi:10.1038/nature00983.1.

906 Lindley, S. T., R. R. Bidigare, and R. T. Barber (1995), Phytoplankton photosynthesis parameters along 140°W in the
907 equatorial Pacific, *Deep Sea Res. II*, *42*(2–3), 441–463.

908 Loisel, H., and A. Morel (1998), Light scattering and chlorophyll concentration in case 1 waters: A reexamination, *Limnol.*
909 *Oceanogr.*, *43*(5), 847–858.

910 Loisel, H., J.-M. Nicolas, P.-Y. Deschamps, and R. Frouin (2002), Seasonal and inter-annual variability of particulate organic
911 matter in the global ocean, *Geophys. Res. Lett.*, *29*(24), 2196, doi:1029/2002GL015948,.

912 Loisel, H., X. Mériaux, J.-F. Berthon, and A. Poteau (2007), Investigation of the optical backscattering to scattering ratio of
913 marine particles in relation to their biogeochemical composition in the eastern English Channel and southern North
914 Sea, *Limnol. Oceanogr.*, *52*(2), 739–752, doi:10.4319/lo.2007.52.2.0739.

915 Loisel, H. et al. (2011), Characterization of the bio-optical anomaly and diurnal variability of particulate matter, as seen from
916 scattering and backscattering coefficients, in ultra-oligotrophic eddies of the Mediterranean Sea, *Biogeosciences*,
917 *8*(11), 3295–3317, doi:10.5194/bg-8-3295-2011.

918 Ludwig, W., E. Dumont, M. Meybeck, and S. Heussner (2009), River discharges of water and nutrients to the Mediterranean
919 and Black Sea: Major drivers for ecosystem changes during past and future decades?, *Prog. Oceanogr.*, *80*(3–4), 199–
920 217, doi:10.1016/j.pocean.2009.02.001.

921 Lutz, V. A., S. Sathyendranath, E. J. H. Head, and W. K. W. Li (2003), Variability in pigment composition and optical

characteristics of phytoplankton in the Labrador Sea and the Central North Atlantic, *Mar. Ecol. Prog. Ser.*, *260*, 1–18, doi:10.3354/meps260001.

MacIntyre, H. L., T. M. Kana, T. Anning, and R. J. Geider (2002), Photocclimation of photosynthesis irradiance response curves and photosynthetic pigments in microalgae and cyanobacteria, *J. Phycol.*, *38*(1), 17–38, doi:10.1046/j.1529-8817.2002.00094.x.

Maritorena, S., D. a Siegel, and A. R. Peterson (2002), Optimization of a semianalytical ocean color model for global-scale applications., *Appl. Opt.*, *41*(15), 2705–2714, doi:10.1364/AO.41.002705.

Marty, J. C., and J. Chiavérini (2010), Hydrological changes in the Ligurian Sea (NW Mediterranean, DYFAMED site) during 1995-2007 and biogeochemical consequences, *Biogeosciences*, *7*(7), 2117–2128, doi:10.5194/bg-7-2117-2010.

Mayot, N., F. D'Ortenzio, M. R. D'Alcalà, H. Lavigne, and H. Claustre (2016), Interannual variability of the Mediterranean trophic regimes from ocean color satellites, *Biogeosciences*, *13*(6), 1901–1917, doi:10.5194/bg-13-1901-2016.

Mendes, C. R. B., R. Kerr, V. M. Tavano, F. A. Cavalheiro, C. A. E. Garcia, D. R. G. Dessai, and N. Anilkumar (2015), Cross-front phytoplankton pigments and chemotaxonomic groups in the Indian sector of the Southern Ocean, *Deep Sea Res. II*, 1–12, doi:10.1016/j.dsr2.2015.01.003.

Mignot, A., H. Claustre, J. Uitz, A. Poteau, F. D. Ortenzio, and X. Xing (2014), Understanding theseasonal dynamics of phytoplankton biomass and the deep chlorophyll maximum in oligotrophic environments: A Bio-Argo float investigation, *Global Biogeochem. Cycles*, *28*(8), 1–21, doi:10.1002/2013GB004781.

Mitchell, B. G. (1992), Predictive bio-optical relationships for polar oceans and marginal ice zones, *J. Mar. Syst.*, *3*(1–2), 91–105, doi:10.1016/0924-7963(92)90032-4.

Mitchell, B. G., and O. Holm-Hansen (1991), Bio-optical properties of Antarctic Peninsula waters: differentiation from temperate ocean models, *Deep Sea Res.*, *38*(8–9), 1009–1028, doi:10.1016/0198-0149(91)90094-V.

Morel, A., and Y. Ahn (1991), Optics of heterotrophic nanoftagellates and ciliates: A tentative assessment of their scattering role in oceanic waters compared to those of bacterial and algal cells, *J. Mar. Res.*, *49*, 177–202.

Morel, A., and J.-F. Berthon (1989), Surface pigments, algal biomass profiles, and potential production of the euphotic layer: Relationships reinvestigated in view of remote-sensing applications, *Limnol. Oceanogr.*, *34*(8), 1545–1562, doi:10.4319/lo.1989.34.8.1545.

Morel, A., and A. Bricaud (1986), Inherent optical properties of algal cells including picoplankton: Theorical and experimental results, *Can. Bull. Fish. Aquat. Sci.*, *214*, 521–559.

Morel, A., and S. Maritorena (2001), Bio-optical properties of oceanic waters: A reappraisal, *J. Geophys. Res.*, *106*(C4), 7163, doi:10.1029/2000JC000319.

952 Morel, A., H. Claustre, D. Antoine, and B. Gentili (2007), Natural variability of bio-optical properties in Case 1 waters:
953 attenuation and reflectance within the visible and near-UV spectral domains, as observed in South Pacific and
954 Mediterranean waters, *Biogeosciences*, *4*(4), 913–925, doi:10.5194/bgd-4-2147-2007.

955 Navarro, G., S. Alvain, V. Vantrepotte, and I. E. Huertas (2014), Identification of dominant phytoplankton functional types in
956 the Mediterranean Sea based on a regionalized remote sensing approach, *Remote Sens. Environ.*, *152*, 557–575,
957 doi:10.1016/j.rse.2014.06.029.

958 Organelli, E., M. Barbieux, H. Claustre, C. Schmechtig, A. Poteau, A. Bricaud, J. Uitz, F. D'Ortenzio, and G. Dall'Olmo
959 (2016a), A global bio-optical database derived from Biogeochemical Argo float measurements within the layer of
960 interest for field and remote ocean colour applications, *SEANOE*, doi:10.17882/47142.

961 Organelli, E., H. Claustre, A. Bricaud, C. Schmechtig, A. Poteau, X. Xing, L. Prieur, F. D'Ortenzio, G. Dall'Olmo, and V.
962 Vellucci (2016b), A novel near real-time quality-control procedure for radiometric profiles measured by Bio-Argo
963 floats: protocols and performances, *J. Atmos. Ocean. Technol.*, *33*, 937–951, doi:10.1175/JTECH-D-15-0193.1.

964 Organelli, E., F. D'Ortenzio, H. Claustre, A. Bricaud, M. Barbieux, J. Uitz, and G. Dall'Olmo (2017a), Bio-optical anomalies
965 in the world's oceans: An investigation on the diffuse attenuation coefficients for downward irradiance derived
966 fromBiogeochemical Argo float measurements, *J. Geophys. Res. Ocean.*, *122*, 2017–2033,
967 doi:doi:10.1002/2016JC012629.

968 Organelli, E. et al. (2017b), Two databases derived from BGC-Argo float measurements for marine biogeochemical and bio-
969 optical applications, *Earth Syst. Sci. Data*, *9*, 861–880, doi:https://doi.org/10.5194/essd-2017-58.

970 Oubelkheir, K., H. Claustre, A. Sciandra, and M. Babin (2005), Bio-optical and biogeochemical properties of different
971 trophic regimes in oceanic waters, *Limnol. Oceanogr.*, *50*(6), 1795–1809, doi:10.4319/lo.2005.50.6.1795.

972 Proctor, C. W., and C. S. Roesler (2010), New insights on obtaining phytoplankton concentration and composition from in
973 situ multispectral Chlorophyll fluorescence, *Limnol. Oceanogr. Methods*, *8*(12), 695–708,
974 doi:10.4319/lom.2010.8.0695.

975 Prospero, J. M. (1996), The Atmospheric Transport of Particles to the Ocean, *Scope-scientific Comm. Probl. Environ. Int.*
976 *Counc. Sci. unions*, *57*, 19–52.

977 Ras, J., H. Claustre, and J. Uitz (2008), Spatial variability of phytoplankton pigment distributions in the Subtropical South
978 Pacific Ocean: comparison between in situ and predicted data, *Biogeosciences*, *5*, 353–369, doi:10.5194/bgd-4-3409-
979 2007.

980 Reynolds, R. a., D. Stramski, and B. G. Mitchell (2001), A chlorophyll-dependent semianalytical reflectance model derived
981 from field measurements of absorption and backscattering coefficients within the Southern Ocean, *J. Geophys. Res.*,
982 *106*(C4), 7125–7138, doi:10.1029/1999JC000311.

983 Riser, S. C., and K. S. Johnson (2008), Net production of oxygen in the subtropical ocean., *Nature*, *451*(7176), 323–325,
984 doi:10.1038/nature06441.

985 Roesler, C. et al. (2017), Recommendations for obtaining unbiased chlorophyll estimates from in situ chlorophyll
986 fluorometers: A global analysis of WET Labs ECO sensors, *Limnol. Oceanogr. Methods*, *15*(6), 572–585,
987 doi:10.1002/lom3.10185.

988 Roesler, C. S., and A. H. Barnard (2013), Optical proxy for phytoplankton biomass in the absence of photophysiology:
989 Rethinking the absorption line height, *Methods Oceanogr.*, *7*, 79–94, doi:10.1016/j.mio.2013.12.003.

990 Sammartino, M., A. Di Cicco, S. Marullo, and R. Santoleri (2015), Spatio-temporal variability of micro-, nano- and pico-
991 phytoplankton in the Mediterranean Sea from satellite ocean colour data of SeaWiFS, *Ocean Sci.*, *11*, 759–778,
992 doi:10.5194/os-11-759-2015.

993 Sathyendranath, S., V. Stuart, A. Nair, K. Oka, T. Nakane, H. Bouman, M. H. Forget, H. Maass, and T. Platt (2009), Carbon-
994 to-chlorophyll ratio and growth rate of phytoplankton in the sea, *Mar. Ecol. Prog. Ser.*, *383*, 73–84,
995 doi:10.3354/meps07998.

996 Schmechtig, C., H. Claustre, A. Poteau, and F. D'Ortenzio (2014), Bio-Argo quality control manual for the Chlorophyll-A
997 concentration, *Argo Data Manag.*, 1–13, doi:doi:10.13155/35385.

998 Schmechtig, C., A. Poteau, H. Claustre, F. D'Ortenzio, G. Dall'Olmo, and E. Boss (2016), Processing Bio-Argo particle
999 backscattering at the DAC level Version, *Argo Data Manag.*, 1–13, doi:doi:10.13155/39459.

1000 Siegel, D. A., S. Maritorena, N. B. Nelson, and M. J. Behrenfeld (2005), Independence and interdependencies among global
1001 ocean color properties: Reassessing the bio-optical assumption, *J. Geophys. Res. C Ocean.*, *110*(7), 1–14,
1002 doi:10.1029/2004JC002527.

1003 Siegel, D. A. et al. (2013), Regional to global assessments of phytoplankton dynamics from the SeaWiFS mission, *Remote*
1004 *Sens. Environ.*, *135*, 77–91, doi:10.1016/j.rse.2013.03.025.

1005 Siokou-Frangou, I., U. Christaki, M. G. Mazzocchi, M. Montresor, M. Ribera d'Alcalá, D. Vaqué, and a. Zingone (2010),
1006 Plankton in the open Mediterranean Sea: a review, *Biogeosciences*, *7*(5), 1543–1586, doi:10.5194/bg-7-1543-2010.

1007 Smith, R. C., and K. S. Baker (1978a), Optical classification of natural waters, *Limnol. Oceanogr.*, *23*(2), 260–267,
1008 doi:10.4319/lo.1978.23.2.0260.

1009 Smith, R. C., and K. S. Baker (1978b), The bio-optical state of ocean waters and remote sensing, *Limnol. Oceanogr.*, *23*(2),
1010 247–259, doi:10.4319/lo.1978.23.2.0247.

1011 Staehr, P. A., P. Henriksen, and S. Markager (2002), Photoacclimation of four marine phytoplankton species to irradiance
1012 and nutrient availability, *Mar. Ecol. Prog. Ser.*, *238*, 47–59, doi:10.3354/meps238047.

1013 Stramska, M., D. Stramski, R. Hapter, S. Kaczmarek, and J. Ston (2003), Bio-optical relationships and ocean color
1014 algorithms for the north polar region of the Atlantic, *J. Geophys. Res.*, *108*(C5), 2156–2202,
1015 doi:10.1029/2001JC001195.

1016 Stramski, D., R. A. Reynolds, M. Kahru, B. G. Mitchell, D. Stramski, R. A. Reynolds, M. Kahru, and B. G. Mitchell (1999),
1017 Estimation of Particulate Organic Carbon in the Ocean from Satellite Remote Sensing, *Science (80-.).*, *285*(5425),
1018 239–242.

1019 Stramski, D., A. Bricaud, and A. Morel (2001), Modeling the inherent optical properties of the ocean based on the detailed
1020 composition of the planktonic community, *Appl. Opt.*, *40*(18), 2929–2945, doi:10.1364/AO.40.002929.

1021 Stramski, D., E. Boss, D. Bogucki, and K. J. Voss (2004), The role of seawater constituents in light backscattering in the
1022 ocean, *Prog. Oceanogr.*, *61*(1), 27–56, doi:10.1016/j.pocean.2004.07.001.

1023 Stramski, D. et al. (2008), Relationships between the surface concentration of particulate organic carbon and optical
1024 properties in the eastern South Pacific and eastern Atlantic Oceans, *Biogeosciences*, *5*(1), 171–201, doi:10.5194/bg-5-
1025 171-2008.

1026 Sullivan, J., M. S. Twardowski, J. Ronald, V. Zaneveld, and C. C. Moore (2013), Measuring optical backscattering in water,
1027 in *Light Scattering Reviews 7*, edited by A. A. Kokhanovsky, pp. 189–224, Springer, Berlin.

1028 Szeto, M., P. J. Werdell, T. S. Moore, and J. W. Campbell (2011), Are the world's oceans optically different?, *J. Geophys.*
1029 *Res.*, *116*(C7), C00H04, doi:10.1029/2011JC007230.

1030 Tanhua, T., D. Hainbucher, K. Schroeder, V. Cardin, M. Álvarez, and G. Civitarese (2013), The Mediterranean Sea system: a
1031 review and an introduction to the special issue, *Ocean Sci.*, *9*(5), 789–803, doi:10.5194/os-9-789-2013.

1032 Taylor, J. R., and R. Ferrari (2010), Buoyancy and Wind-Driven Convection at Mixed Layer Density Fronts, *J. Phys.*
1033 *Oceanogr.*, *40*(6), 1222–1242, doi:10.1175/2010JPO4365.1.

1034 Uitz, J., H. Claustre, A. Morel, and S. B. Hooker (2006), Vertical distribution of phytoplankton communities in open ocean:
1035 An assessment based on surface chlorophyll, *J. Geophys. Res.*, *111*, C08005, doi:10.1029/2005JC003207.

1036 Uitz, J., H. Claustre, F. B. Griffiths, J. Ras, N. Garcia, and V. Sandroni (2009), A phytoplankton class-specific primary
1037 production model applied to the Kerguelen Islands region (Southern Ocean), *Deep Sea Res. I*, *56*(4), 541–560,
1038 doi:10.1016/j.dsr.2008.11.006.

1039 Vaillancourt, R. D., C. W. Brown, R. R. L. Guillard, and W. M. Balch (2004), Light backscattering properties of marine
1040 phytoplankton: relationships to cell size, chemical composition and taxonomy, *J. Plankton Res.*, *26*(2), 191–212,
1041 doi:10.1093/plankt/fbh012.

1042 Volk, T., and M. I. Hoffert (1985), Ocean Carbon Pumps: Analysis of relative strengths and efficiencies in ocean-driven

1043 atmospheric C02 changes, in *The Carbon Cycle and Atmospheric CO_2: Natural Variations Archean to Present*, vol.
1044 32, edited by E. T. Sundquist and W. S. Broecker, pp. 99–110, Geophysical Monograph Series, Washington, D. C.

1045 Westberry, T. K., M. J. Behrenfeld, P. Schultz, J. P. Dunne, M. R. Hiscock, S. Maritorena, J. L. Sarmiento, and D. A. Siegel
1046 (2016), Annual cycles of phytoplankton biomass in the subarctic Atlantic and Pacific Ocean, *Global Biogeochem.*
1047 *Cycles*, *30*(2), 175–190, doi:10.1002/2015GB005276.

1048 Whitmire, A. L., W. S. Pegau, L. Karp-Boss, E. Boss, and T. J. Cowles (2010), Spectral backscattering properties of marine
1049 phytoplankton cultures, *Opt. Express*, *18*(14), 15073–15093, doi:10.1029/2003RG000148.D.

1050 Winn, C. D., L. Campbell, J. R. Christian, R. M. Letelier, D. V Hebel, J. E. Dore, L. Fujieki, and D. M. Karl (1995), Seasonal
1051 variability in the phytoplankton community of the North Pacific Subtropical Gyre, *Global Biogeochem. Cycles*, *9*(4),
1052 605–620, doi:10.1029/95gb02149.

1053 Wong, A., R. Keeley, and T. Carval (2013), Argo quality control manual, *Argo Data Manag.*, 1–50, doi:doi:10.13155/33951.

1054 Xing, X., A. Morel, H. Claustre, D. Antoine, F. D'Ortenzio, A. Poteau, and A. Mignot (2011), Combined processing and
1055 mutual interpretation of radiometry and fluorimetry from autonomous profiling Bio-Argo floats: Chlorophyll a
1056 retrieval, *J. Geophys. Res.*, *116*(C6), C06020, doi:10.1029/2010JC006899.

1057 Xing, X., H. Claustre, S. Blain, F. D'Ortenzio, D. Antoine, J. Ras, and C. Guinet (2012), Quenching correction for in vivo
1058 chlorophyll fluorescence acquired by autonomous platforms: A case study with instrumented elephant seals in the
1059 Kerguelen region (Southern Ocean), *Limnol. Oceanogr.*, *10*, 483–495, doi:10.4319/lom.2012.10.483.

1060 Xing, X., H. Claustre, J. Uitz, A. Mignot, A. Poteau, and H. Wang (2014), Seasonal variations of bio-optical properties and
1061 their interrelationships observed by Bio-Argo floats in the subpolar North Atlantic, *J. Geophys. Res.*, *119*, 1–17,
1062 doi:10.1002/2014JC010189.

1063 Xing, X., H. Claustre, E. Boss, C. Roesler, E. Organelli, A. Poteau, M. Barbieux, and F. D'Ortenzio (2016), Correction of
1064 profiles of in-situ chlorophyll fluorometry for the contribution of fluorescence originating from non-algal matter,
1065 *Limnol. Oceanogr. Methods*, *15*(1), 80–93, doi:10.1002/lom3.10144.

1066 Yentsch, C. S., and D. a. Phinney (1989), A bridge between ocean optics and microbial ecology, *Limnol. Oceanogr.*, *34*(8),
1067 1694–1705, doi:10.4319/lo.1989.34.8.1694.

1068 Zhang, X., L. Hu, and M.-X. He (2009), Scattering by pure seawater: Effect of salinity, *Opt. Express*, *17*(7), 5698–5710,
1069 doi:10.1364/OE.17.012685.

1070

Figure 1.

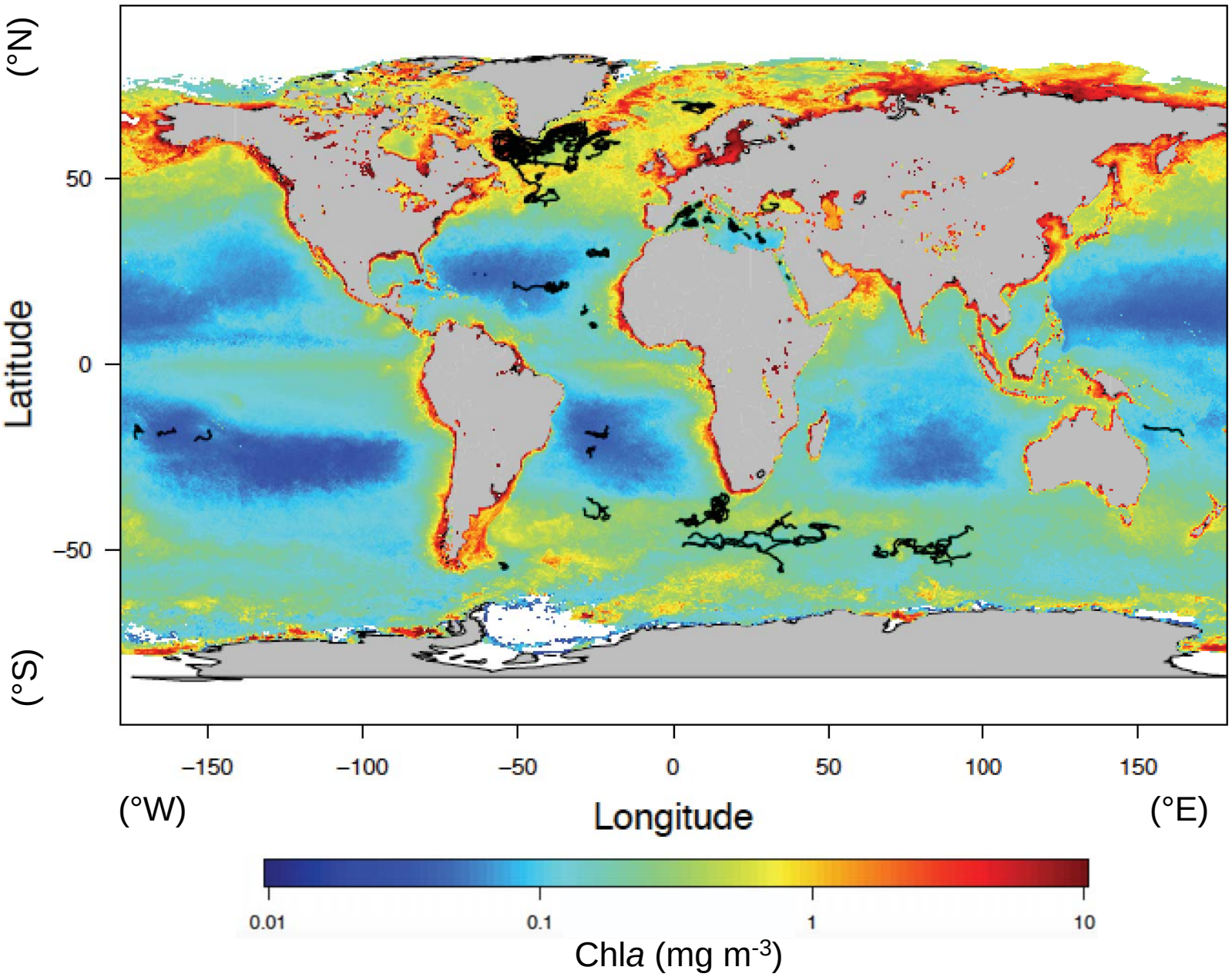
(°N)
50
0
−50
(°S)
Latitude
−150
−100
−50
0
50
100
150
(°W)
Longitude
(°E)
0.01
0.1
1
10
Chl*a* (mg m^{-3})

Figure 2.

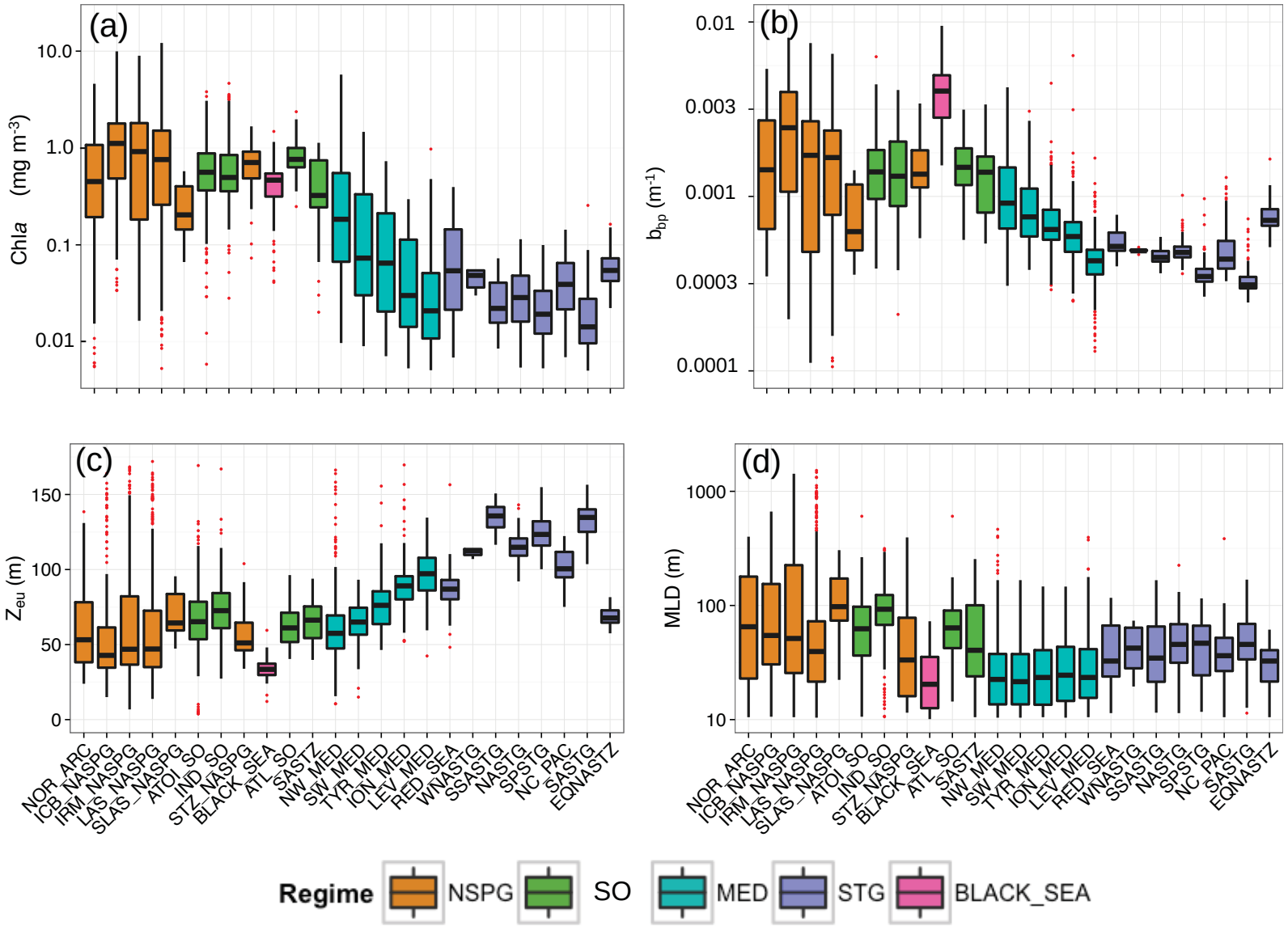
(a)
Chla (mg m-3)
10.0
1.0
0.1
0.01
(b)
bbp (m-1)
0.01
0.003
0.001
0.0003
0.0001
(c)
Zeu (m)
150
100
50
0
(d)
MLD (m)
1000
100
10
NOR_ARC
ICB_NASPG
IRM_NASPG
LAS_NASPG
SLAS_NASPG
ATOI_SO
IND_SO
STZ_NASPG
BLACK_SEA
ATL_SO
SASTZ
NW_MED
SW_MED
TYR_MED
ION_MED
LEV_MED
RED_SEA
WNASTG
SSASTG
NASTG
SPSTG
NC_PAC
SASTG
EQNASTZ
Regime
NSPG
SO
MED
STG
BLACK_SEA

Figure 3.

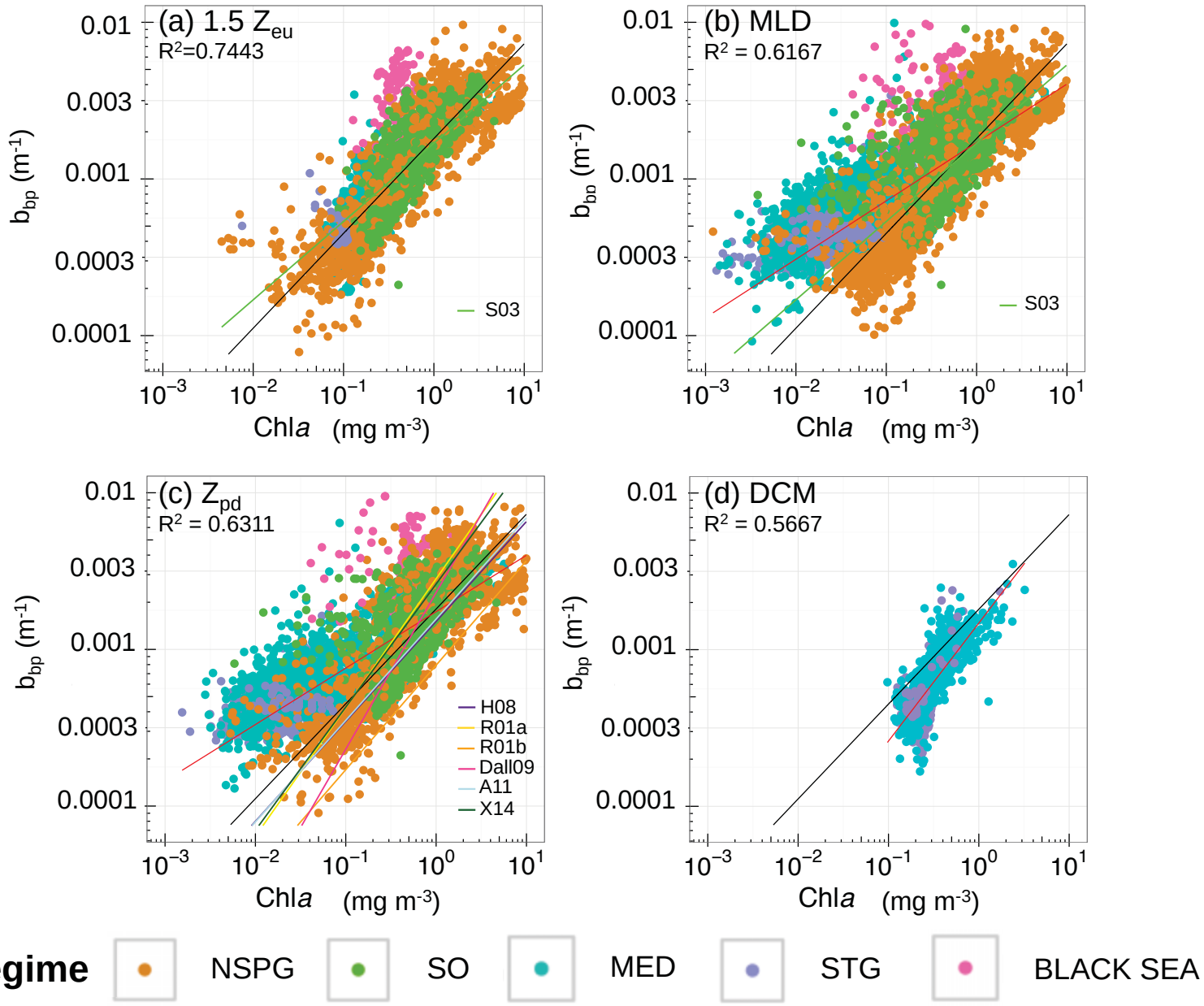
(a) 1.5 Zeu
R²=0.7443
(b) MLD
R² = 0.6167
(c) Zpd
R² = 0.6311
(d) DCM
R² = 0.5667
S03
H08
R01a
R01b
Dall09
A11
X14
bbp (m-1)
Chla (mg m-3)
Regime
NSPG
SO
MED
STG
BLACK SEA

Figure 4.

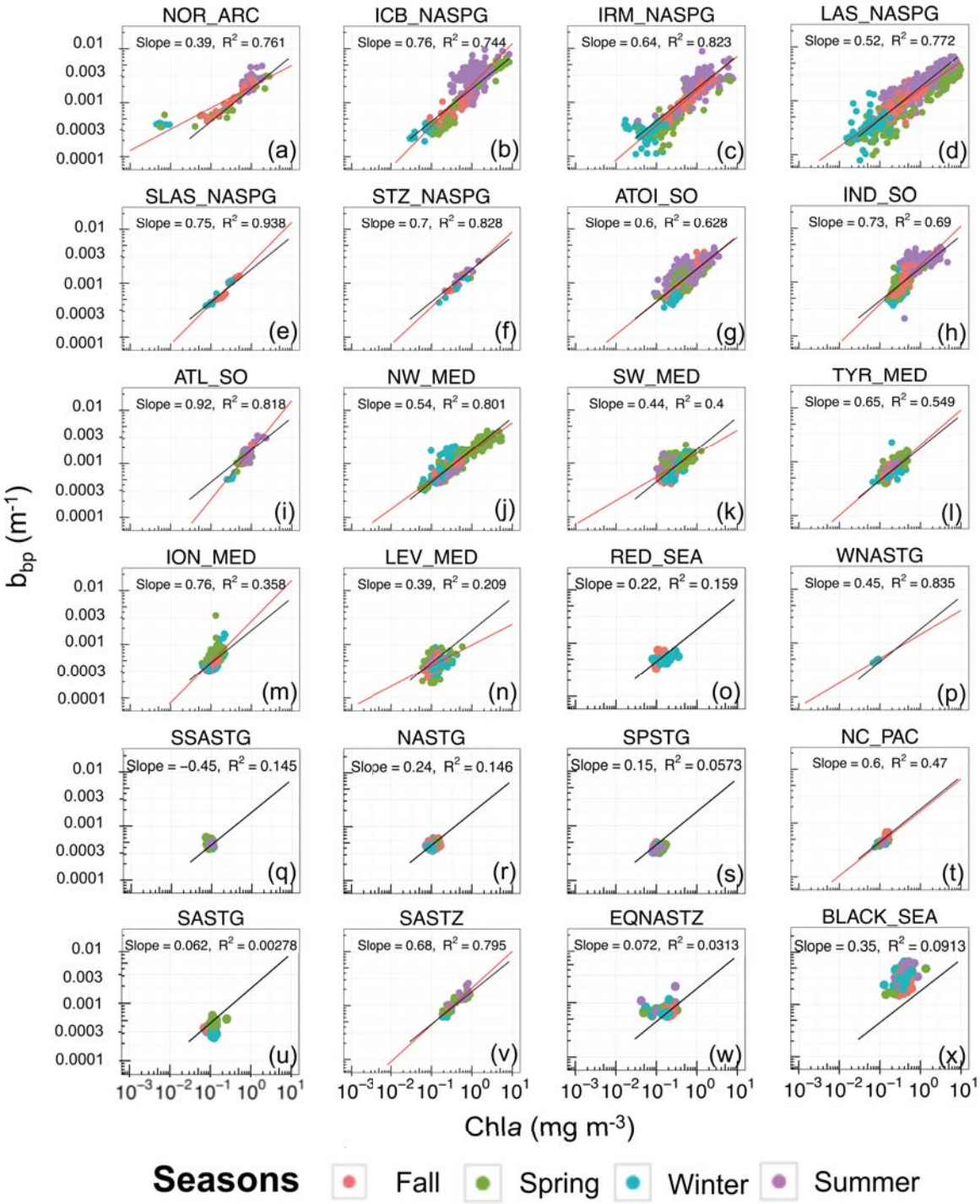
NOR_ARC
Slope = 0.39, R² = 0.761
(a)
ICB_NASPG
Slope = 0.76, R² = 0.744
(b)
IRM_NASPG
Slope = 0.64, R² = 0.823
(c)
LAS_NASPG
Slope = 0.52, R² = 0.772
(d)
SLAS_NASPG
Slope = 0.75, R² = 0.938
(e)
STZ_NASPG
Slope = 0.7, R² = 0.828
(f)
ATOI_SO
Slope = 0.6, R² = 0.628
(g)
IND_SO
Slope = 0.73, R² = 0.69
(h)
ATL_SO
Slope = 0.92, R² = 0.818
(i)
NW_MED
Slope = 0.54, R² = 0.801
(j)
SW_MED
Slope = 0.44, R² = 0.4
(k)
TYR_MED
Slope = 0.65, R² = 0.549
(l)
ION_MED
Slope = 0.76, R² = 0.358
(m)
LEV_MED
Slope = 0.39, R² = 0.209
(n)
RED_SEA
Slope = 0.22, R² = 0.159
(o)
WNASTG
Slope = 0.45, R² = 0.835
(p)
SSASTG
Slope = −0.45, R² = 0.145
(q)
NASTG
Slope = 0.24, R² = 0.146
(r)
SPSTG
Slope = 0.15, R² = 0.0573
(s)
NC_PAC
Slope = 0.6, R² = 0.47
(t)
SASTG
Slope = 0.062, R² = 0.00278
(u)
SASTZ
Slope = 0.68, R² = 0.795
(v)
EQNASTZ
Slope = 0.072, R² = 0.0313
(w)
BLACK_SEA
Slope = 0.35, R² = 0.0913
(x)
0.01
0.003
0.001
0.0003
0.0001
10^{-3} 10^{-2} 10^{-1} 10^{0} 10^{1}
b_{bp} (m^{-1})
Chla (mg m^{-3})
Seasons
Fall
Spring
Winter
Summer

Figure 5.

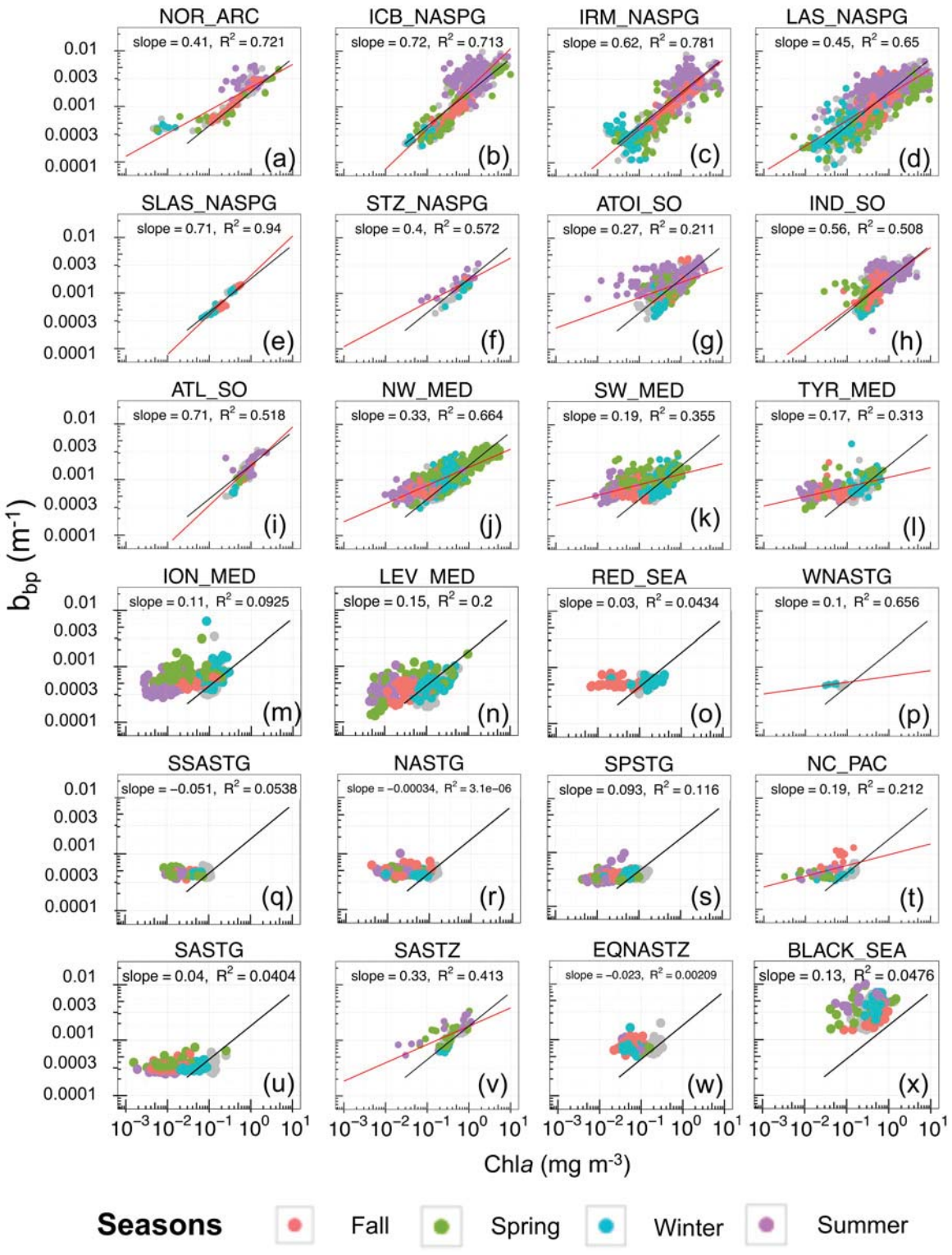
NOR_ARC
slope = 0.41, R2 = 0.721
(a)
ICB_NASPG
slope = 0.72, R2 = 0.713
(b)
IRM_NASPG
slope = 0.62, R2 = 0.781
(c)
LAS_NASPG
slope = 0.45, R2 = 0.65
(d)
SLAS_NASPG
slope = 0.71, R2 = 0.94
(e)
STZ_NASPG
slope = 0.4, R2 = 0.572
(f)
ATOI_SO
slope = 0.27, R2 = 0.211
(g)
IND_SO
slope = 0.56, R2 = 0.508
(h)
ATL_SO
slope = 0.71, R2 = 0.518
(i)
NW_MED
slope = 0.33, R2 = 0.664
(j)
SW_MED
slope = 0.19, R2 = 0.355
(k)
TYR_MED
slope = 0.17, R2 = 0.313
(l)
ION_MED
slope = 0.11, R2 = 0.0925
(m)
LEV_MED
slope = 0.15, R2 = 0.2
(n)
RED_SEA
slope = 0.03, R2 = 0.0434
(o)
WNASTG
slope = 0.1, R2 = 0.656
(p)
SSASTG
slope = −0.051, R2 = 0.0538
(q)
NASTG
slope = −0.00034, R2 = 3.1e−06
(r)
SPSTG
slope = 0.093, R2 = 0.116
(s)
NC_PAC
slope = 0.19, R2 = 0.212
(t)
SASTG
slope = 0.04, R2 = 0.0404
(u)
SASTZ
slope = 0.33, R2 = 0.413
(v)
EQNASTZ
slope = −0.023, R2 = 0.00209
(w)
BLACK_SEA
slope = 0.13, R2 = 0.0476
(x)
bbp (m-1)
0.01
0.003
0.001
0.0003
0.0001
10−3 10−2 10−1 100 101
Chla (mg m-3)
Seasons
Fall
Spring
Winter
Summer

Figure 6.

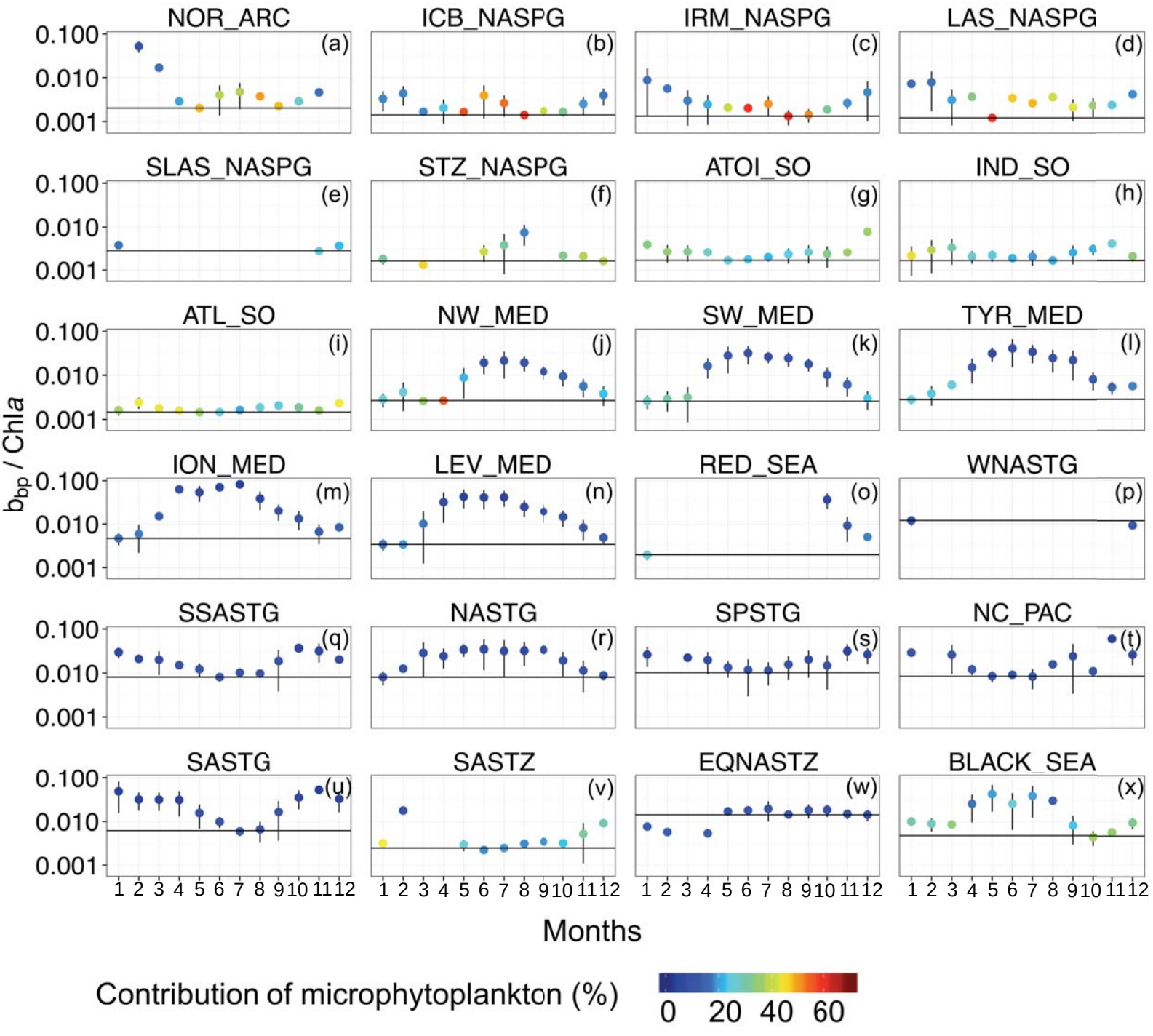
NOR_ARC
(a)
ICB_NASPG
(b)
IRM_NASPG
(c)
LAS_NASPG
(d)
SLAS_NASPG
(e)
STZ_NASPG
(f)
ATOI_SO
(g)
IND_SO
(h)
ATL_SO
(i)
NW_MED
(j)
SW_MED
(k)
TYR_MED
(l)
ION_MED
(m)
LEV_MED
(n)
RED_SEA
(o)
WNASTG
(p)
SSASTG
(q)
NASTG
(r)
SPSTG
(s)
NC_PAC
(t)
SASTG
(u)
SASTZ
(v)
EQNASTZ
(w)
BLACK_SEA
(x)
0.100
0.010
0.001
1 2 3 4 5 6 7 8 9 10 11 12
b_{bp} / Chl*a*
Months
Contribution of microphytoplankton (%)
0 20 40 60

Figure 7.

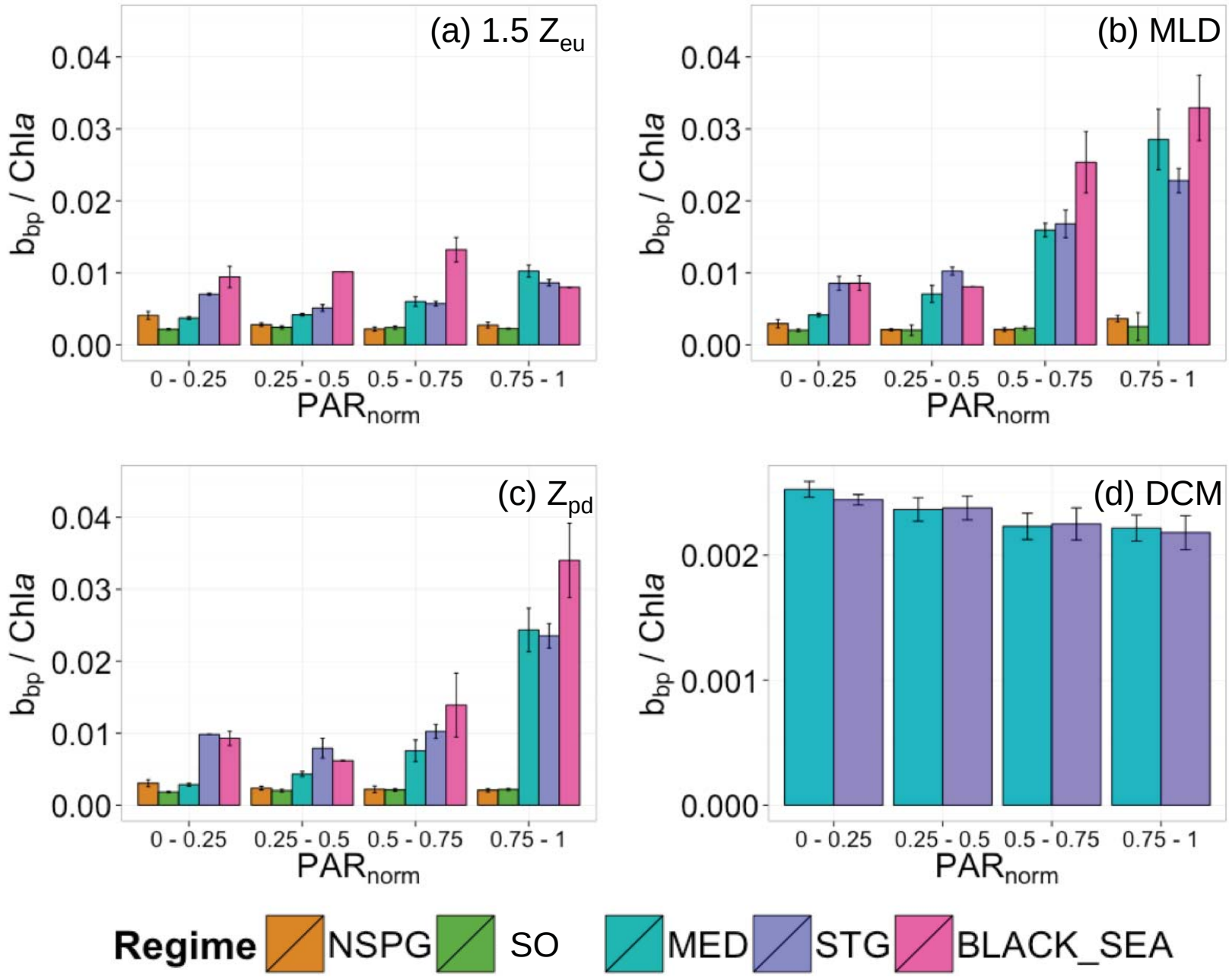
(a) 1.5 Z_{eu}
(b) MLD
(c) Z_{pd}
(d) DCM
b_{bp} / Chla
0.04
0.03
0.02
0.01
0.00
0.002
0.001
0.000
0 - 0.25
0.25 - 0.5
0.5 - 0.75
0.75 - 1
PAR_{norm}
Regime
NSPG
SO
MED
STG
BLACK_SEA

Figure 8.

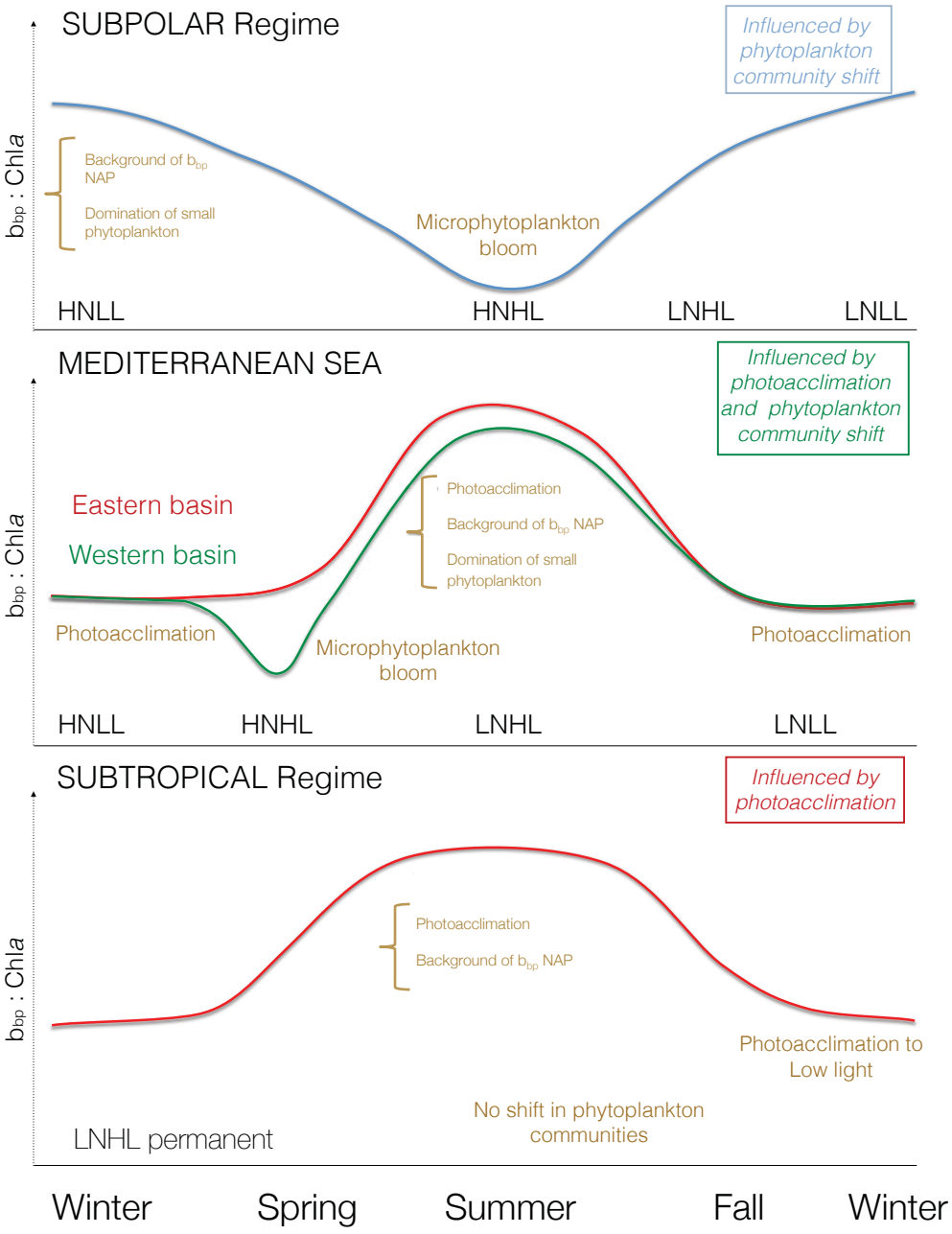
SUBPOLAR Regime
Influenced by phytoplankton community shift
b_{bp} : Chl*a*
Background of b_{bp} NAP
Domination of small phytoplankton
Microphytoplankton bloom
HNLL
HNHL
LNHL
LNLL
MEDITERRANEAN SEA
Influenced by photoacclimation and phytoplankton community shift
Eastern basin
Western basin
Photoacclimation
Background of b_{bp} NAP
Domination of small phytoplankton
Photoacclimation
Microphytoplankton bloom
Photoacclimation
HNLL
HNHL
LNHL
LNLL
SUBTROPICAL Regime
Influenced by photoacclimation
Photoacclimation
Background of b_{bp} NAP
Photoacclimation to Low light
No shift in phytoplankton communities
LNHL permanent
Winter
Spring
Summer
Fall
Winter

***Table 1** . Bioregions with the corresponding abbreviation, regime and number of available floats and profiles represented in the BGC-Argo database used in the present study.*

Location	Region abbreviation	N° profiles	N° floats
NORWEGIAN_SEA	NOR_ARC	139	1
ICELAND BASIN	ICB_NASPG	828	8
IRMINGER SEA	IRM_NASPG	623	11
LABRADOR SEA	LAS_NASPG	1160	16
SOUTH OF LABRADOR SEA	SLAS_NASPG	62	2
ATLANTIC TO INDIAN SOUTHERN OCEAN	ATOI_SO	910	10
INDIAN SECTOR OF SOUTHERN OCEAN	IND_SO	653	6
NORTH ATLANTIC TO SUB TROPICAL GYRE TRANSITION ZONE	STZ_NASPG	146	1
BLACK SEA	BLACK_SEA	141	2
ATLANTIC SECTOR OF SOUTHERN OCEAN	ATL_SO	49	1
SOUTH ATLANTIC SUB TROPICAL TRANSITION ZONE	SASTZ	214	2
LIGURIAN SEA & GULF OF LIONS	NW_MED	698	8
PROVENCAL & ALGERO PROVENCAL	SW_MED	417	4
TYRRHENIAN SEA	TYR_MED	325	5
IONIAN SEA	ION_MED	499	6
LEVANTINE SEA	LEV_MED	511	7
RED SEA	RED_SEA	75	2
NORTH ATLANTIC WESTERN SUB TROPICAL GYRE	WNASTG	12	2
SOUTH ATLANTIC SOUTH SUB TROPICAL GYRE	SSASTG	108	1
NORTH ATLANTIC SUB TROPICAL GYRE	NASTG	363	4
SOUTH PACIFIC SUB TROPICAL GYRE	SPSTG	281	3
NEW CALEDONIA	NC_PAC	139	2
UTH ATLANTIC SUB TROPICAL GY	SASTG	368	2
NORTH ATLANTIC TO EQUATOR SUB TROPICAL TRANSITION ZONE	EQNASTZ	187	2
TOTAL		8908	108

Table 2. *Empirical relationship between the particulate backscattering coefficient (b_{bp}) and the c previously published in the literature with the corresponding reference and abbreviation, regi considered for analysis.*

Regression formula	Region	Layer in the water column	Abbreviation
$b_{bp}(\lambda) = 2.267 \times 10^{-3} - 5.058 \times 10^{-6} (\lambda - 550) \times (Chla)^{0.565+0.000486*(\lambda-550)}$	Eastern South Pacific	$2/K_d(490)$	H08
$b_{bp}(555) = 0.004 \times (Chla)^{0.822}$	Antarctic Polar Front	15m	R01a
$b_{bp}(555) = 0.001 \times (Chla)^{0.667}$	Ross Sea	15m	R01b
$b_{bp}(555) = 0.0019 \times (Chla)^{0.61}$	Polar North Atlantic	MLD	S03
$b_{bp}(526) = 0.00386*(Chla)$	Eastern Equatorial Pacific	Surface	Dall09
$b_{bp}(532) = 0.003*(Chla)^{0.786}$	North Atlantic Subpolar Gyre	Z_{pd}	X14
$b_{bp}(555) = 0.00197 \times (Chla)^{0.647}$	North-western Mediterranean Sea and Santa Barbara Channel	Surface	A11

concentration of chlorophyll a (Chla)
ion and layer of the water column

Reference
Huot et al. (2008)
Reynolds et al. (2001)
Reynolds et al. (2001)
Stramska et al. (2003)
Dall'Olmo et al. (2009) modified in Xing et al. (2014)
Xing et al. (2014)
Antoine et al. (2011)

Table 3 *. Empirical relationships obtained between the particulate backscattering coefficient (b_{bp}) and the concentration of chlorophyll a (Chla) for the different layers of the water column considered in this study. We also indicate the associated statistics: Root Mean Squared Error (RMSE) and coefficient of determination R^2 for the significance level of $p < 0.001$*

Empirical relationship	Layer in the water column	R^2	RMSE	Number of data
$b_{bp}(700) = 0.00174 \times (Chla)^{0.360}$	Z_{pd}	0.6311	0.000942	5253
$b_{bp}(700) = 0.00171 \times (Chla)^{0.373}$	MLD	0.6167	0.000932	8743
$b_{bp}(700) = 0.00147 \times (Chla)^{0.753}$	DCM	0.5667	0.00104	1628
$b_{bp}(700) = 0.00181 \times (Chla)^{0.605}$	$1.5 \times Z_{eu}$	0.7443	0.000967	5250